

**PROCESSING OF NANOCOMPOSITES AND THEIR THERMAL AND  
RHEOLOGICAL CHARACTERIZATION**

by

**Jacob M. Faulkner**

**A Thesis**

*Submitted to the Faculty of Purdue University*

*In Partial Fulfillment of the Requirements for the degree of*

**Master of Science in Mechanical Engineering**



School of Mechanical Engineering

West Lafayette, Indiana

August 2019

**THE PURDUE UNIVERSITY GRADUATE SCHOOL  
STATEMENT OF COMMITTEE APPROVAL**

Dr. Xiulin Ruan, Chair

School of Mechanical Engineering

Dr. George T.-C. Chiu

School of Mechanical Engineering

Dr. Liang Pan

School of Mechanical Engineering

**Approved by:**

Dr. Eckhard Groll

Head of the Graduate Program

## ACKNOWLEDGMENTS

First and foremost, I want to thank my advisor, Prof. Xiulin Ruan, for not only giving me my first chance at research, but also continuing to support and believe in me throughout my professional journey. Without Prof. Ruan's immense knowledge and exceptional mentorship, I would not be the first in my family to earn a graduate degree. Prof. Ruan has helped me develop into a competent researcher and a superior individual as I attempted to replicate his passion, drive, and warm, light-hearted nature. His guidance has allowed me to continuously improve to the point that I am now able to complete my research and thesis. It is both a privilege and honor to have worked with Prof. Ruan, and I know that wherever my career path takes me I will be prepared because of his personal and professional mentorship.

Next, I would like to extend my gratitude to my committee members Prof. George T.-C. Chiu and Prof. Liang Pan for their wisdom and continued support during my thesis work. I especially want to thank Prof. Chiu for extending his lab and resources as well as Jie Wang for his printing expertise in collaboration. I also thank Prof. Amy Marconnet and Prof. Mukerrem Cakmak for aiding my research by providing me the use of their experimental equipment.

I thank my entire research group for their critiques and discussions, especially Dr. Xiangyu Li who has mentored me since I was an undergraduate student. Xiangyu's generous and freely-given knowledge and advice greatly bolstered my research and education.

Last, but certainly not least I would like to thank my family and fiancé Catherine for their loving encouragement and unwavering backing of myself and my goals.

## TABLE OF CONTENTS

LIST OF TABLES .....	6
LIST OF FIGURES .....	7
NOMENCLATURE .....	9
ABSTRACT.....	13
1. INTRODUCTION .....	14
1.1 Thermal Conductivity Modeling with Filler.....	15
1.1.1 Maxwell’s Model.....	16
1.1.2 Hashin-Shtrikman Model.....	17
1.1.3 Nan’s Model .....	17
1.1.4 Multiple-Level EMAs.....	18
1.2 Rheological Characterization of Nanocomposites.....	19
1.2.1 Viscosity Background.....	20
1.2.2 Intrinsic Viscosity .....	22
1.2.3 Viscosity Modeling with Filler.....	22
1.2.3.1 Einstein’s Model.....	23
1.2.3.2 Kreiger-Dougherty Model .....	23
1.2.3.3 Batchelor’s Model .....	24
1.2.3.4 Chen’s Model .....	24
1.2.4 Surface Tension .....	25
1.3 Objectives and Organization of Thesis .....	25
2. FEASABILITY ANALYSIS OF 3D PRINTING THERMAL INTERFACE MATERIALS ..	
.....	27
2.1 3D Printing Techniques of PDMS .....	27
2.1.1 Fused Deposition Modeling.....	28
2.1.2 Conformal .....	28
2.1.3 Stereolithography.....	29
2.1.4 Direct Ink Writing.....	29
2.2 Graphene Nanoplatelet Particle Selection .....	30

2.3	Sample Preparation .....	32
2.4	Viscosity Measurement Technique .....	33
2.5	Experimental Viscosity of PDMS with GNP .....	33
2.6	Modeling of Viscosity.....	41
2.7	Printability of Samples.....	56
2.8	Thermal Conductivity Measurement Technique .....	57
2.9	Modeling of Thermal Conductivity .....	58
3.	PRINTING OF RADIATIVE COOLING INK.....	59
3.1	Techniques for Printing Ink versus Paint.....	59
3.1.1	Brush Coating .....	60
3.1.2	Inkjet .....	60
3.1.3	Screen Printing.....	60
3.2	Nanocomposite Printing of Radiative Cooling Paint.....	61
3.3	Radiative Cooling Viscosity .....	63
3.4	Printed Performance of Radiative Cooling Paint.....	65
	REFERENCES .....	68

## LIST OF TABLES

Table 1: Solvent selection parameters. ....	62
---	----

## LIST OF FIGURES

Figure 1: Fluid flowing between two parallel plates commonly known as planar Couette flow.	20
Figure 2: Shear stress as a function of shear rate for different types of materials.	21
Figure 3: The measured viscosity as a function of the shear rate for each PDMS component and the mixed weight ratios of SE 1700: Sylgard 184.	34
Figure 4: Viscoelastic effects of SE 1700 give rise to a larger uncertainty in the results.	35
Figure 5: Cleaner data for Sylgard 184 is due to its more fluidic properties.	36
Figure 6: The measured viscosity as a function of shear rate for the lowest tested concentration of GNP filler at different PDMS ratios.	37
Figure 7: The measured viscosity as a function of shear rate for low GNP filler loadings at different PDMS ratios.	38
Figure 8: The measured viscosity as a function of shear rate for 2.5 wt. % GNP loading at different PDMS ratios.	39
Figure 9: The measured viscosity as a function of shear rate for a moderate graphene loading of 5 wt. % at different PDMS ratios.	39
Figure 10: The measured viscosity as a function of shear rate for the highest tested GNP loadings.	41
Figure 11: Intrinsic viscosity fitting for 5:5 PDMS ratio at a shear rate of $10 \text{ s}^{-1}$ .	43
Figure 12: Viscosity model fitting to the experimental data of 5:5 PDMS ratio with GNP filler at a shear rate of $10 \text{ s}^{-1}$ .	44
Figure 13: Intrinsic viscosity fitting for 5:5 PDMS ratio at a shear rate of $60 \text{ s}^{-1}$ .	45
Figure 14: Viscosity model fitting to the experimental data of 5:5 PDMS ratio with GNP filler at a shear rate of $60 \text{ s}^{-1}$ .	45
Figure 15: Intrinsic viscosity fitting for 6:4 PDMS ratio at a shear rate of $10 \text{ s}^{-1}$ .	46
Figure 16: Viscosity model fitting to the experimental data of 6:4 PDMS ratio with GNP filler at a shear rate of $10 \text{ s}^{-1}$ .	47
Figure 17: Intrinsic viscosity fitting for 6:4 PDMS ratio at a shear rate of $60 \text{ s}^{-1}$ .	48
Figure 18: Viscosity model fitting to the experimental data of 6:4 PDMS ratio with GNP filler at a shear rate of $60 \text{ s}^{-1}$ .	48

Figure 19: Intrinsic viscosity fitting for 7:3 PDMS ratio at a shear rate of $10 \text{ s}^{-1}$ . .....	49
Figure 20: Viscosity model fitting to the experimental data of 7:3 PDMS ratio with GNP filler at a shear rate of $10 \text{ s}^{-1}$ . .....	50
Figure 21: Intrinsic viscosity fitting for 7:3 ratio PDMS at a shear rate of $60 \text{ s}^{-1}$ . .....	51
Figure 22: Viscosity models from literature fit to the experimental data for 7:3 ratio PDMS with GNP filler at a constant shear rate of $60 \text{ s}^{-1}$ . .....	51
Figure 23: Intrinsic viscosity fitting for 8:2 ratio PDMS at a shear rate of $10 \text{ s}^{-1}$ . .....	52
Figure 24: Viscosity models from literature fit to the experimental data for 8:2 ratio PDMS with GNP filler at a constant shear rate of $10 \text{ s}^{-1}$ . .....	53
Figure 25: Intrinsic viscosity fit for a PDMS ratio of 8:2 at a shear rate of $60 \text{ s}^{-1}$ . .....	54
Figure 26: Viscosity model fitting of experimental data for 8:2 ratio PDMS with GNP filler at a constant shear rate of $60 \text{ s}^{-1}$ . .....	54
Figure 27: Viscosity model fitting of experimental data for low GNP concentrations of 7:3 ratio PDMS at a constant shear rate of $10 \text{ s}^{-1}$ . .....	55
Figure 28: Discrepancy between the fitting of only $\phi ma$ with both $\phi ma$ and $\phi m$ for the Chen model to experimental data. ....	56
Figure 29: Samples with GNP filler that fall within the printable viscosity range using Chen's model with two fit parameters as well as all experimental data points measured in this work. ...	57
Figure 30: Drop-on-demand inkjet printing setup for radiative cooling paint processing. ....	61
Figure 31: Screen printing setup for processing of radiative cooling paint samples. ....	63
Figure 32: Viscosity as a function of shear rate for the radiative cooling paint sample with 60 vol. % $\text{BaSO}_4$ and toluene solvent. ....	64
Figure 33: Viscosity as a function of shear rate for commercial paints with different matrix materials [75]. ....	64
Figure 34: Screen printing of radiative cooling paint pattern onto a) barium sulfate coated art paper and b) commercial printer paper. ....	65
Figure 35: IR camera image of the screen-printed radiative cooling paint with very little temperature difference compared to the commercial printing paper substrate. ....	66
Figure 36: Radiative properties of the baryte paper substrate. ....	67
Figure 37: Radiative properties of the commercial printer paper substrate. ....	67

## NOMENCLATURE

$a$	radii
$A$	cross-sectional area
$c$	specific heat
$c$	filler concentration
$D$	fractal index
$F$	force
$H$	gap height
$k, K$	thermal conductivity
$L$	object length
$L_{ii}$	particle geometric factor
$n$	shape factor
$p$	aspect ratio of ellipsoid
$q$	rate of heat transfer
$q''$	heat flux
$r$	aspect ratio
$R$	radius of the cone
$T$	total torque
$\Delta T$	temperature drop
$\nabla T$	temperature gradient
$u$	velocity of fluid
$U_0$	velocity of top plate
$V$	porosity
$v_g$	group velocity
$[\eta]$	intrinsic viscosity
$\alpha$	interaction fitting parameter
$\alpha$	absorption
$\beta$	intermediate variable
$\dot{\gamma}$	shear rate

$\theta$	angle between particle and matrix axis
$\theta$	angle of the cone
$\mu, \eta$	viscosity
$\rho$	reflection
$\tau$	phonon relaxation time
$\tau$	shear stress
$\tau$	transmission
$\chi$	volume fraction
$\omega$	angular velocity
$\phi$	volume concentration
$\phi_m$	maximum volume fraction of filler

#### Subscripts

0	base fluid
1	matrix
2	filler
$a$	aggregates
$c$	cluster
$e$	effective
eff	effective
$f$	filler
$H$	Huggins
$i$	intrinsic
$ii$	coordinate
inh	inherent
$K$	Kraemer
$m$	matrix
$ma$	packing fraction of aggregates
$p$	particle
$r$	relative

red	reduced
<i>s</i>	Solomon-Ciuta
<i>sp</i>	specific
$\lambda$	phonon frequency

### Superscripts

*	effective
<i>c</i>	equivalent
lower	lower bound
upper	upper bound

### Abbreviations

ABS	acrylonitrile butadiene styrene
BTE	Boltzmann transport equation
CAD	computer-aided-design
CNC	computer numerical control
DIW	direct ink writing
DMF	dimethylformamide
EMA	effective medium approximation
FDM	fused deposition modeling
GNP	graphene nanoplatelet
HS	Hashin-Shtrikman
IR	infrared
KD	Krieger-Dougherty
MEK	methyl ethyl ketone
MG	Maxwell-Garnett
PDMS	polydimethylsiloxane
PLA	polylactic acid
TIM	thermal interface material

UV	ultraviolet
vol.	volume
wt.	weight

## ABSTRACT

Author: Faulkner, Jacob, M. MSME

Institution: Purdue University

Degree Received: August 2019

Title: Processing of Nanocomposites and their Thermal and Rheological Characterization

Committee Chair: Xiulin Ruan

Polymer nanocomposites are a constantly evolving material category due to the ability to engineer the mechanical, thermal, and optical properties to enhance the efficiency of a variety of systems. While a vast amount of research has focused on the physical phenomena of nanoparticles and their contribution to the improvement of such properties, the ability to implement these materials into existing commercial or newly emerging processing methods has been studied much less extensively. The primary characteristic that determines which processing technique is the most viable is the rheology or viscosity of the material. In this work, we investigate the processing methods and properties of nanocomposites for thermal interface and radiative cooling applications. The first polymer nanocomposite examined here is a two-component PDMS with graphene filler for 3D printing via a direct ink writing approach. The composite acts as a thermal interface material which can enhance cooling between a microprocessor and a heat sink by increasing the thermal conductivity of the gap. Direct ink writing requires a shear thinning ink with specific viscoelastic properties that allow for the material to yield through a nozzle as well as retain its shape without a mold following deposition. No predictive models of viscosity for nanocomposites exist; therefore, several prominent models from literature are fit with experimental data to describe the change in viscosity with the addition of filler for several different PDMS ratios. The result is an understanding of the relationship between the PDMS component ratio and graphene filler concentration with respect to viscosity, with the goal of remaining within the acceptable limits for printing via direct ink writing. The second nanocomposite system whose processability is determined is paint consisting of acrylic filled with reflective nanoparticles for radiative cooling paint applications. The paint is tested with both inkjet and screen-printing procedures with the goal of producing a thermally invisible ink. Radiative cooling paint is successfully printed for the first time with solvent modification. This work evaluates the processability of polymer nanocomposites through rheological tailoring.

## 1. INTRODUCTION

Nanomaterial design is of immense importance to scientists and engineers due to the vast array of applications and the ability to alter material properties to desired specifications. A particularly promising division of nanomaterials includes polymer matrices filled with dispersed particles that have a characteristic length on the order of nanometers ( $10^{-9}$  m), known as polymer nanocomposites. The physics and predictive modeling of nanocomposites has proven to be very challenging due to the characteristic size being smaller than the typical mean free path of energy carriers. Nanomaterials are used to increase the overall efficiency of systems with applications including corrosion resistance, increased heat transfer in electronics, as well as improved mechanical and optical performance [1]. This work focuses on two specific applications of nanocomposites, namely thermal interface materials (TIMs) and radiative cooling paints.

As the processing power of electronics continues to increase, the demand to remove excess heat progressively intensifies. TIMs fill the air gap between an electronic heat generator and a heat sink to increase conductive heat transfer and maintain lower device temperatures, while typically providing electrical insulation. These lower temperatures lead to increases in the lifetime and performance of electronics. Polymer nanocomposites are a popular material for TIMs due to the electrical insulation from the polymer matrix along with the enhanced thermal conductivity provided by the nanoparticle fillers. However, thermal enhancement often comes at the price of rheological enhancement, making samples harder to process. Specifically, the 3D printing technique of direct ink writing requires a precise operating range of viscosity in which the sample can be extruded through a nozzle while retaining the desired shape after deposition. This work designs a TIM for 3D printing by direct ink writing by examining and modeling the enhancement to viscosity of the filler.

Radiative cooling paint can be used to decrease the temperature of outdoor surfaces, which is useful for outdoor electronics or reduction of building cooling costs. The paint passively cools by reflecting sunlight primarily from 0.3-2.5  $\mu\text{m}$  and emitting through the transparent spectral window of the atmosphere, or “sky window”, from 8 to 13  $\mu\text{m}$ . The paint requires nanoparticles sized near the peak of the solar spectrum to scatter the sunlight and achieve full daytime cooling below ambient temperatures. Rheological characteristics of this substance can be easily controlled by adjusting the solvent concentration, which has no effect on the optical

performance, allowing for the employment of both ink and paint-based processing techniques. This work focuses on the automated printing of a radiative cooling paint whose optical design and cooling performance was developed previously by Li et al. [2].

### 1.1 Thermal Conductivity Modeling with Filler

Thermal conductivity,  $k$ , of a material characterizes its ability to transmit heat and is defined as [3]

$$k = \frac{q \cdot L}{A \cdot \Delta T}, \quad 1$$

where  $q$  is the rate of heat flow,  $L$  is the object length,  $A$  is the cross-sectional area and  $\Delta T$  is the temperature drop across the sample. The classical equation to determine thermal conductivity is Fourier's law, specified by

$$q'' = -k \nabla T, \quad 2$$

where  $q''$  is the heat flux,  $k$  is the thermal conductivity, and  $\nabla T$  is the temperature gradient across the sample. A high thermal conductivity in dielectrics is required to maintain lower temperatures in thermal management, while a low thermal conductivity leads to higher efficiencies in thermoelectric devices [4].

A more contemporary view of thermal conductivity in dielectric materials is that the thermal transport is dominated by atomic lattice vibrations, phonons, with negligible contribution of electrons at room temperature. The second order force constant and dynamical matrix are used to solve for the allowable phonon frequencies and dispersion relation. At each frequency there is a specific energy, propagating speed, and scattering rate that determines the overall thermal conductivity. This approach calculates thermal conductivity as

$$k = \sum_{\lambda} c_{\lambda} v_{g,\lambda}^2 \tau_{\lambda}, \quad 3$$

where  $\lambda$  is the phonon frequency,  $c_{\lambda}$  is the phonon specific heat,  $v_g$  is the group velocity, and  $\tau_{\lambda}$  is the phonon relaxation time [5]. Equation (3) describes thermal conductivity by the single-mode relaxation time approximation of the Boltzmann Transport Equation (BTE) that assumes a similar form to Fourier's law. However, direct calculation proves impossible for most composite materials due to a randomly orientated and distributed filler material. The BTE neglects the wave nature of electrons and phonons by regarding them as classical particles, which can lead to inaccuracies due to increased wave interference since phonon wavelengths and nanoscale particles are on the same order of magnitude [6]. The BTE also assumes the system is near

equilibrium and there exists a local temperature, approximations that are both invalid at length scales below the mean free path of phonons [6]. Additionally, these methods fail to account for Kapitza resistance, or the thermal boundary resistance, between two dissimilar materials, which becomes important in nanocomposites due to the vast number of interfaces [7]. Kapitza resistance corresponds to the transmission and scattering of phonons at interfaces, and it lowers thermal conductivity when compared to bulk samples. Computer simulations such as Monte Carlo or Molecular Dynamics can be used to solve the BTE; however, large computational costs are required unless major simplifications, including periodic boundary conditions, are made, thereby reducing accuracy. The following effective medium approximations (EMAs) have been developed to describe the thermal conductivity for a homogenous macroscopic system full of complex microscopic processes.

### 1.1.1 Maxwell's Model

The Maxwell model is a classical description for thermal conductivity of heterogeneous mixtures. The basis of the model and its adaptations is the groundbreaking work of Maxwell [8]. The Maxwell-Garnett (MG) model for predicting the dielectric function of glass containing micron-sized spherical particles was one of the first EMA models proposed. This provides the basis of many later works but only accounts for isolated spherical particles [9]. Hamilton and Crosser applied Maxwell's work to produce an EMA that accounted for non-spherical particle shapes as

$$K = K_1 \left[ \frac{K_2 + (n-1)K_1 - (n-1)V_2(K_1 - K_2)}{K_2 + (n-1)K_1 + V_2(K_1 - K_2)} \right], \quad 4$$

where  $K$  is the thermal conductivity of the mixture,  $K_1$  is the thermal conductivity of the matrix,  $K_2$  is the thermal conductivity of the filler,  $n$  is dependent on the shape of the filler, and  $V_2$  is the volume fraction of air or porosity [10]. The value for  $n$  is a constant value of 3 when solved in spherical coordinates for spherical particles and 6 for cylindrical particles, meaning the shape factor is independent of particle size as well as the values of  $K_1$  and  $K_2$  in these cases [10]. The model is verified through comparison with experimental data of various shapes of aluminum and balsa particles inside of Silastic rubber, but fails to account for interfacial resistance, the anisotropy of the material, or any particle interactions. The MG model was extended to thermal conductivity with the inclusion of thermal boundary resistance by Hasselman and Johnson and

shows good agreement below 40 volume percent of filler while accounting for isolated particles of spherical, cylindrical, and flat plate shapes [11],[12].

### 1.1.2 Hashin-Shtrikman Model

A bounded solution for multiphase materials with isotropic filler is presented by Hashin and Strinkman (HS) for magnetic permeability, but due to mathematical relations also extends to the dielectric function, electrical conductivity, and thermal conductivity [13]. The HS model derivation provides the most restrictive bounds for two-phase macroscopically homogeneous samples. For the case of a low thermal conductivity polymer matrix and high conductivity filler, the lower bound describes completely isolated filler particles surrounded by matrix material. The upper bound consists of a connected network structure of filler particles. The HS model upper and lower bound are described by the following equations [14].

$$k_{eff}^{upper} = k_f \frac{2k_f + k_m - 2\chi_m(k_f - k_m)}{2k_f + k_m + \chi_m(k_f - k_m)} \quad 5$$

$$k_{eff}^{lower} = k_m \frac{2k_m + k_f - 2\chi_f(k_m - k_f)}{2k_m + k_f + \chi_f(k_m - k_f)} \quad 6$$

Here  $k_f$  is the filler thermal conductivity,  $k_m$  is the matrix thermal conductivity,  $\chi_f$  is the filler volume fraction, and  $\chi_m$  is the matrix volume fraction. The location of the measured thermal conductivity within the two bounds can give an estimation of the degree to which the fillers are interconnected. A pathway of linked filler creates the most ideal pathway for heat transfer. This EMA does not consider filler shape, or anisotropy, but is one of the few models that accounts for interaction between individual filler particles, which establishes the two solution boundaries.

### 1.1.3 Nan's Model

The comprehensive work of Nan et al. presents an EMA based on multiple-scattering theory that accounts for particle size, orientation, size distribution, shape, and Kapitza resistance [15]. The formulation of a two-phase composite containing ellipsoidal particles is given by

$$K_{11}^* = K_{22}^* = K_m \frac{2+f[\beta_{11}(1-L_{11})(1+\langle \cos^2 \theta \rangle) + \beta_{33}(1-L_{33})(1-\langle \cos^2 \theta \rangle)]}{2-f[\beta_{11}L_{11}(1+\langle \cos^2 \theta \rangle) + \beta_{33}L_{33}(1-\langle \cos^2 \theta \rangle)]} \quad 7$$

$$K_{33}^* = K_m \frac{1+f[\beta_{11}(1-L_{11})(1-\langle \cos^2 \theta \rangle) + \beta_{33}(1-L_{33})(\langle \cos^2 \theta \rangle)]}{1-f[\beta_{11}L_{11}(1-\langle \cos^2 \theta \rangle) + \beta_{33}L_{33}(\langle \cos^2 \theta \rangle)]} \quad 8$$

and

$$\beta_{ii} = \frac{K_{ii}^c - K_m}{K_m + L_{ii}(K_{ii}^c - K_m)} \quad 9$$

$$L_{11} = L_{22} = \frac{p^2}{2(p^2-1)} - \frac{p}{2(1-p^2)^{\frac{3}{2}}} \cosh^{-1} p, \text{ for } p < 1 \quad 10$$

$$L_{33} = 1 - 2L_{11}, \quad 11$$

where  $\theta$  is the angle between the particle and matrix axis,  $L_{ii}$  is a particle geometric factor,  $K_m$  is the matrix thermal conductivity, and  $K_p$  is the particle thermal conductivity [15]. The value of  $\langle \cos^2 \theta \rangle$  is 1/3 for randomly oriented particles which can reduce the equation to

$$K^* = K_m \frac{3+f[2\beta_{11}(1-L_{11})+\beta_{33}(1-L_{33})]}{3-f[2\beta_{11}L_{11}+\beta_{33}L_{33}]} \quad 12$$

The model is verified with experimental results for diamond/ZnS, SiC/Al, and diamond/cordierite composites, but fails to account for any effects caused by the differences in aggregation of particles.

#### 1.1.4 Multiple-Level EMAs

Multiple-level EMAs have been successfully developed and implemented to nanocomposite systems by breaking down the complete process into distinct components and accounting for the dominate physical phenomena in each segment of the system. The multiple-level models have shown significantly better agreement with experimental data than the classical models that underpredict thermal conductivity of nanocomposites. This technique has been utilized by Evans et al. with a three-level homogenization model that calculates thermal conductivity based on certain characteristics of nanoparticle aggregation [16]. The particles are modeled as long linear chains called backbones that extend through the entire cluster along with various particles that only attach to parts of the chain called dead ends [16]. The thermal conductivity of dead-end particles are found using the Bruggeman symmetric model, which has shown accurate results for high volume concentrations due to accounting for particle interactions and the percolation threshold; however, it is limited to spherical particles and does not account for interfacial resistance [12],[17]. The thermal conductivity of the linear backbone chains is found from Nan's model for randomly oriented cylindrical particles [16]. Finally, the thermal conductivity of the macroscopic system is found using the MG model with the utilized concentration and thermal conductivity value being that of the nanoparticle clusters.

A two-level EMA was developed by Li et al. to account for particle size and aggregation characteristics of nanoparticles [18]. The first level calculates the thermal conductivity of closely packed aggregates by using the upper bound of the HS model, while the second level assumes

spherical and isolated clusters that can be found from the Maxwell model as

$$k_e = k_m \frac{k_c + 2k_m + 2\phi_c(k_c - k_m)}{k_c + 2k_m - \phi_c(k_c - k_m)}, \quad 13$$

where  $k_c$  is the thermal conductivity of the clusters found from the first level of the EMA,  $k_e$  is the effective thermal conductivity of the sample,  $k_m$  is the thermal conductivity of the matrix, and  $\phi_c$  is the volume concentration of nanoparticle clusters [18]. While the Evans et al. EMA failed to predict accurate values for this system, Li's two-level model was able to account for the increase in thermal conductivity shown in smaller particle sizes at the same volume concentration for TIMs consisting of an epoxy matrix filled with 10, 20, 70, and 1,500 nm diameter nickel spheres [18]. The increase in thermal conductivity in the smaller sized particles was due to more dispersed particle clustering that created a more efficient path for heat [18]. These works have shown that aggregation effects, accounted for in multiple-level EMA models, are a dominating factor in the thermal conductivity of nanocomposite TIMs.

## 1.2 Rheological Characterization of Nanocomposites

Perhaps the most important material characteristic related to processing feasibility is the substance's rheology. All fluids are defined as materials that continuously deform under the application of a shear stress, a force parallel to the surface of an object. Newtonian fluids, such as water, exhibit simple relations between this input force and their resistance to flow. However, polymers show very different characteristics when subjected to shear forces, including behavior that combines the elastic features of solids with the viscous frictional dissipation of liquids, known as viscoelasticity. Polymers consist of linear and branched chains, which play a vital role in rheological characteristics. For example, the average length of these chains, or molecular weight, is one of the primary factors that determines the viscosity of the substance. Longer chains tend to entangle more, which significantly restricts flow. Moreover, the chains create a shear-thinning behavior because as shear rates increase, the chains begin to align in the direction of flow, thereby decreasing viscosity. Due to viscoelastic effects, polymers can exhibit phenomena that seemingly defy the laws of physics but are understandable with knowledge of their chain structure. These phenomena include the Weissenberg effect, where polymers climb up a rotating shaft similarly to how spaghetti travels up a rotating fork, as well as the open-siphon effect, where only a small stream exiting a vertical beaker empties all fluid from the entire container. The only controllable processing parameter for a fixed material is a change in

the applied shear stress, so precise knowledge of how the fluid will deform and react to this stress is required. In this manner, flow can be precisely manipulated into the desired patterns or shapes of the final design prior to curing the polymer into a solid substance.

### 1.2.1 Viscosity Background

A simple definition of viscosity, a fluid's resistance to shear forces, is defined for a fluid located between two parallel plates separated by a distance,  $H$ . This one-dimensional flow configuration, commonly referred to as planar Couette flow, is illustrated in Fig. 1.

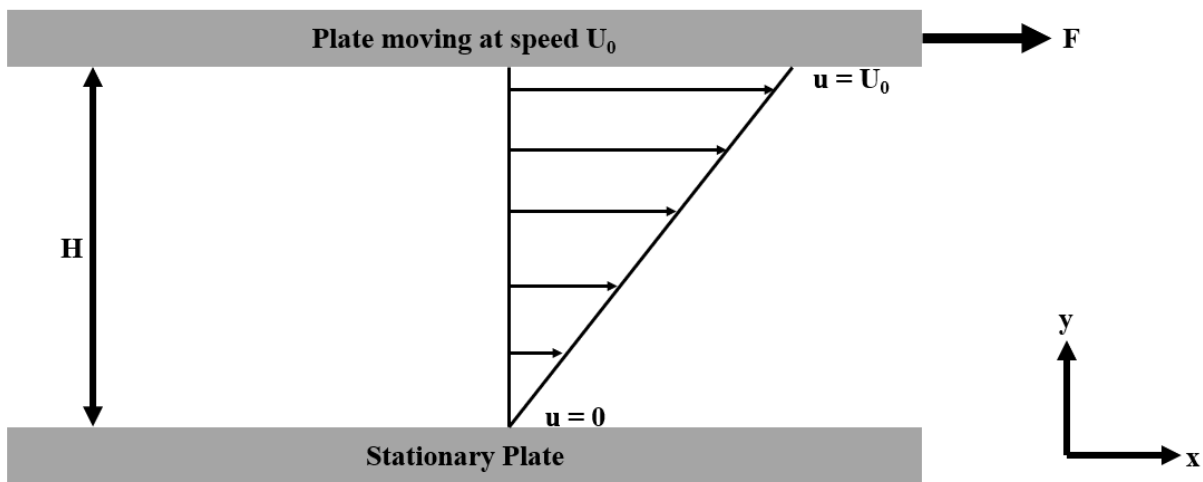


Figure 1: Fluid flowing between two parallel plates commonly known as planar Couette flow.

The shear stress,  $\tau = \frac{F}{A}$ , is imparted on the fluid by the force given to the plate divided by the area of the plate in contact with the fluid. This shear stress causes the top plate to move at velocity  $U_0$ , while the bottom plate remains stationary. Assuming no slip between the fluid and plates, the fluid at the top plate moves at  $U_0$  and the fluid just above the stationary bottom plate has zero velocity. The rate of deformation for the fluid, or shear rate, is defined as the velocity gradient,  $\frac{du}{dy}$ . For Newtonian fluids, there is a simple linear relation between the shear stress and shear rate that is defined by absolute (dynamic) viscosity,  $\mu$ . This formula can be generalized as

$$\tau = \mu \frac{\partial u}{\partial y}, \quad 14$$

commonly known as Newton's law of viscosity, where the units of viscosity are found from the

difference in shear stress [ $\text{N}/\text{m}^2$ ] and shear rate [ $\text{s}^{-1}$ ] to be [ $\text{Pa}\cdot\text{s}$ ] in SI units or poise [ $1 \text{ poise} \equiv 1 \frac{\text{g}}{\text{cm}\cdot\text{s}}$ ] in metric units.

Constant viscosity regardless of the applied shear stress holds for Newtonian fluids like water, but polymers do not follow this trend. The behavior of several non-Newtonian materials is shown in Fig. 2, where viscosity is given by the slope of the curves.

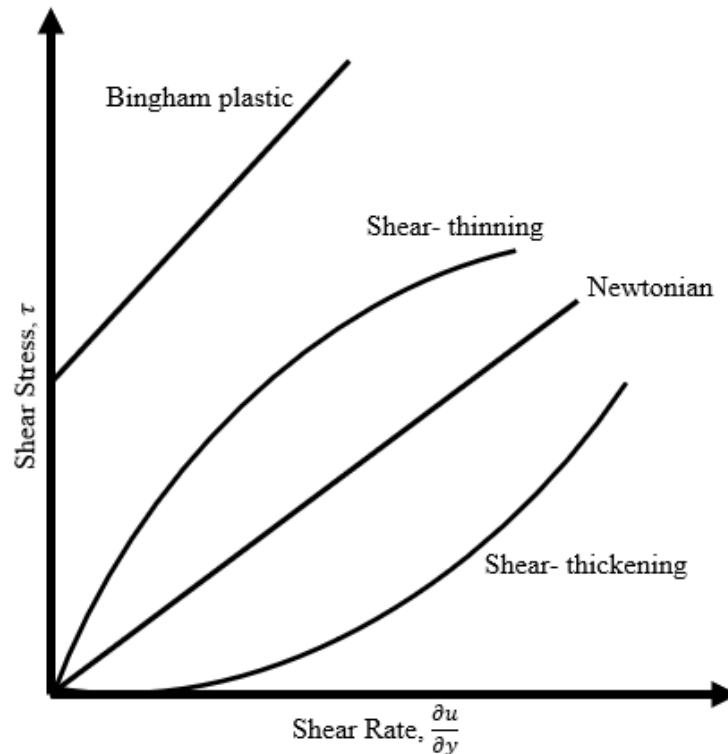


Figure 2: Shear stress as a function of shear rate for different types of materials.

For most non-Newtonian materials, the viscosity of the substance changes based on the applied shear stress. A Bingham plastic shows unique solid-like behavior before a critical yield stress is reached followed by Newtonian flow. An example of this type of material is toothpaste. Shear thickening materials, such as cornstarch and water (oobleck), have increased viscosity at higher shear rates. Many polymers show shear-thinning behavior, where viscosity decreases with increasing shear rates, due to the alignment of anisotropic chains with the direction of shear.

### 1.2.2 Intrinsic Viscosity

Intrinsic viscosity,  $[\eta]$ , characterizes the effect of gradually adding liquid solute or solid filler material into a solution. Some common viscosity terms that are useful for understanding are

$$\eta_r = \frac{\eta}{\eta_0} \quad 15$$

$$\eta_i = \frac{\ln \eta_r}{c} \quad 16$$

$$\eta_{sp} = \frac{\eta - \eta_0}{\eta_0} = \eta_r - 1, \quad 17$$

where  $\eta$  is the solution viscosity,  $\eta_0$  is the solvent viscosity,  $\eta_r$  is the relative viscosity,  $\eta_i$  is the intrinsic viscosity,  $\eta_{sp}$  is the specific viscosity, and  $c$  is the filler concentration with units of g/dL. Viscosity can be expressed as a Taylor series expansion, where the first and second terms are the solvent viscosity and product of the solvent viscosity and intrinsic viscosity, respectively [19].

The early works of Huggins and Kraemer provided two equivalent procedures to extrapolate the value for intrinsic viscosity with multiple data points at low concentration. The intrinsic viscosity is found from [20],[21]

$$[\eta] = \lim_{c \rightarrow 0} \frac{\ln(\eta_r)}{c} = \lim_{c \rightarrow 0} \frac{\eta_{sp}}{c}. \quad 18$$

This method requires linear extrapolation to zero concentration of either the inherent viscosity or the reduced viscosity that is defined as the specific viscosity over the concentration. An Ubbelohde viscometer is a capillary measurement device that utilizes Equation (18) and the Taylor series expansion to determine both the intrinsic viscosity and the relative viscosity of the solution.

Solomon-Ciuta presents a solution technique to determine the intrinsic viscosity from a single measured value at low concentration [22]. The calculation involves

$$[\eta] = \frac{2(\eta_{sp} - \ln(\eta_r))^{\frac{1}{2}}}{c}, \quad 19$$

in which all terms have been previously defined [19], [22]. This technique is required when very limited data is available on the material of interest.

### 1.2.3 Viscosity Modeling with Filler

Nanocomposite viscosity is not only dependent on the base polymer, but it is also heavily influenced by the nano-sized particles that fill the matrix. The modeling of viscosity enhancement due to the addition of filler in suspensions has been studied for over a century

although not as extensively as thermal conductivity. The models generally all consider the viscosity of the base fluid and filler volume concentration. Similar to the models for thermal conductivity based on Maxwell's equations, the classical methods for viscosity initially only account for isolated spherical particles before additional physical effects are accounted for in later models to further enhance agreement with experimental data.

### 1.2.3.1 Einstein's Model

Much of the basis for viscosity of colloidal suspensions is extended from the theoretical work of Einstein's Ph.D. thesis in 1906. Einstein considered a dilute isotropic suspension of uncharged hard spheres within a Newtonian base fluid [23]. The dilute approximation meant that the derivation could be done for the effects of a single particle in an infinite base fluid medium. The resulting equation is

$$\eta_{eff} = \eta_0(1 + [\eta]\phi), \quad 20$$

where  $\eta_{eff}$  is the effective viscosity of the suspension,  $\eta_0$  is the viscosity of the base fluid,  $[\eta]$  is the intrinsic viscosity, and  $\phi$  is the volume concentration of filler particles [23]. For the case of hard spheres, the intrinsic viscosity was found to be a constant value of  $\frac{5}{2}$ . The accuracy of the model only extends to low volume concentrations ( $\phi \leq 0.02$ ) due to the dilute assumption [24]. Einstein's model has since been mathematically proven as a first-order expansion of the effective viscosity as a function of the volume fraction of filler [25]. The model can only account for particle shape and size effects through the intrinsic viscosity parameter and does not consider an interfacial layer.

### 1.2.3.2 Kreiger-Dougherty Model

Kreiger and Dougherty (KD) developed a viscosity model that considers low order interactions between particles. The model first accounts for particles that rotate completely independently, similarly to Einstein's model, called singlets [26]. However, due to random Brownian motion, there will always be spheres that are separated by less than a single diameter and their effect on the flow will be coupled which is referred to as a doublet [26]. This coupling effect will produce particles that rotate together, like a dumbbell, but will be much less prevalent than the singlets due to the shear forces breaking them apart back into singlets [26]. The equation that resulted is

$$\frac{\eta_{eff}}{\eta_0} = \left(1 - \frac{\phi}{\phi_m}\right)^{-[\eta]\phi_m}, \quad 21$$

where the intrinsic viscosity is the same as in Einstein's model with the additional term of  $\phi_m$ , or the maximum volume fraction of filler. The most error for this equation is seen at low-shear and high concentrations where triplet and higher order particle interactions occur.

### 1.2.3.3 Batchelor's Model

Batchelor expanded Equation (20) for rigid spherical particles to include higher order terms due to Brownian motion, which causes higher order particle interactions. Batchelor determined that the hydrodynamic interactions between particles is a second order phenomena. This expansion of Einstein's formulism is

$$\eta_{eff} = \eta_0(1 + [\eta]\phi + \alpha\phi^2), \quad 22$$

where  $\alpha$  is the interaction fitting parameter [24]. The model approaches Einstein's model at very low particle loadings and is valid when  $\phi \leq 0.04$  [27]. All of the presented models so far have shown underprediction of nanofluids relative viscosity, especially when the filler volume percent is greater than 0.04 [27].

### 1.2.3.4 Chen's Model

More recent work by Chen et al. has modified the KD model to consider spherical agglomerates of different sizes. This is a very significant addition, as agglomeration effects have shown a considerable influence on the thermal conductivity of nanocomposites [16], [18]. The general form of the equation is given as

$$\frac{\eta_{eff}}{\eta_0} = \left(1 - \frac{\phi_a}{\phi_m}\right)^{-[\eta]\phi_m}, \quad 23$$

with the only modification to Equation (21) being to change from the volume concentration of particles to the volume concentration of aggregates [28]. This factor is further defined as

$$\phi_a = \frac{\phi}{\phi_{ma}} = \phi \left(\frac{a_a}{a}\right)^{3-D}, \quad 24$$

where  $\phi_{ma}$  is the packing fraction of aggregates,  $a_a$  is the radii of aggregates,  $a$  is the radii of primary nanoparticles, and  $D$  is the fractal index [28]. In this case, the maximum valid particle loading is only limited by the stability of the nanofluid. Furthermore, the aggregation effect of rod and tube-like particle viscosity has also been estimated by Chen et al. by considering the aspect ratio,  $r_a$ , and dividing the ethylene glycol based titanate nanotube fluid into three separate

categories being dilute ( $0 < \phi_a < 1/r_a^2$ ), semi-dilute ( $1/r_a^2 < \phi_a < 1/r_a$ ), and concentrated ( $1/r_a < \phi_a$ ) nanofluids [29]. Each category has a slightly modified calculation procedure.

#### 1.2.4 Surface Tension

The surface tension of a material is the final rheological aspect that must be known for effective processing. The surface tension is often measured using the Young Equation, where the contact angles extending from the three-phase point are used to determine the surface tension of the liquid. Error in this measurement is often encountered due to surface roughness. Surface energy for solids is the equivalent quantity for surface tension in liquids, although it is harder to measure as it requires several contact angle measurements with liquids of known surface tension. Other devices that can measure surface tension include the Du Nouy ring and Wilhelmy plate, which measures the force required to break the surface of a liquid, as well as the max bubble pressure technique, which can determine the dynamic surface tension of samples. In terms of processing, the difference between the sample and substrate surface energy is immensely important as it determines the amount of wetting of the surface. Complete wetting will occur if the surface energies are identical and the entire sample volume will spread out onto the substrate, which is the ideal scenario. The amount of spreading is required to know the precise resolution of any ink-based processing methods.

### 1.3 Objectives and Organization of Thesis

The objective of this work is to understand the viscosity effects on processing of nanocomposite fillers. The first objective is to design a thermal interface material for 3D printing by direct ink writing with a novel approach of exploring the effect of nanocomposite filler on viscosity rather than solely focusing on thermal conductivity. Our unique method attempts to focus primarily on minimizing the enhancement to viscosity to remain printable, while also allowing for the addition of higher concentrations of filler that will in turn lead to the greatest enhancement to thermal conductivity. The target viscosity range is much higher than previously studied because it must retain its shape after 3D printing compared to that of a pure nanofluid. The second objective is to develop a method of automated printing of radiative cooling materials. No other passive radiative cooling device has the large-scale applicability of paint, so automated

applications could further reduce costs and allow for precise application of temperature gradients. The printing method is experimentally verified with inkjet and screen printing.

This thesis is divided into two chapters. Chapter two discusses the analysis performed to determine the optimal thermal interface system for 3D printing. The advantages and disadvantages of several 3D printing methods are examined. Graphene nanoplatelets are selected as a filler material due to their particle shape showing advantageous effects on viscosity. The sample preparation and rheological measurement technique are then outlined. Viscosity results of the PDMS-graphene thermal interface material are presented and compared with mathematical models from literature. A 3D printable range is established based on the composite viscosity. Finally, the thermal conductivity measurement technique is described. Chapter three details the printing of radiative cooling paint. The techniques for printing are outlined and then compared with experimental results. Successful automated printing of radiative cooling paint is demonstrated for the first time. We then examine the viscosity of the paint and performance of the printed samples.

## **2. FEASIBILITY ANALYSIS OF 3D PRINTING THERMAL INTERFACE MATERIALS**

Thermal interface material development is imperative due to the ever-increasing power density of electronic circuits that intensifies the demand for cooling applications. Proper cooling maintains lower temperatures so that suitable performance and product lifetimes are attainable [30]. Traditional manufacturing techniques for nanocomposites require expensive metallic molds that can take several weeks of precise machining to produce, resulting in a high setup cost for any new design [31]. This molding procedure is only practical for mass production to recoup the setup cost with the capability of extremely high throughput rates. However, recent interest in additive manufacturing, or more specifically the subset of 3D printing, has grown due to the possibilities of reducing labor and material costs, increasing resolution, and allowing for easier prototyping with more complex designs [31]. Although current 3D printing is not able to compete with the extremely high throughput rates of injection molded materials, it could allow for much cheaper development of designs in small batches so that the most optimal device could transition to the expensive molded mass manufacturing stage.

The matrix material chosen for the 3D printed TIM is polydimethylsiloxane (PDMS). PDMS is a silicon-based polymer that is thermally stable, biocompatible, non-toxic, non-flammable, and optically transparent [32]. PDMS is selected due to its low cost, wide use for microfluidic and flexible electronic applications, and commonly available viscosity values that are often used to calibrate rheometers. The flexibility of the material is advantageous for completely filling the air gaps between electronic components generated by their surface roughness compared with stiffer matrix polymers such as epoxy [32].

### **2.1 3D Printing Techniques of PDMS**

Additive manufacturing builds products by adding layers of material atop of one another. The objects are most often created in a computer-aided-design (CAD) software and converted through a program that divides the part into individual layers and guides the deposition or solidification head along these spatial guidelines. This additive process is in stark contrast to the traditional computer numerical control (CNC) machining that also converts CAD models to spatial machine code, but instead removes material from a standard billet, thus creating both a

part and scrap waste. Therefore, 3D printing also has the added benefit of utilizing a larger fraction of the material compared with CNC machining, reducing overall production costs. Conventional PDMS manufacturing involves soft-lithography, which suffers from the same drawbacks of other molding practices that primarily involve the high cost of creating an initial master mold [31]. To characterize which 3D printing process is the most optimal for developing a TIM, each popular process will be reviewed and assessed for its ability to create PDMS nanocomposites.

### **2.1.1 Fused Deposition Modeling**

The most common commercially available 3D printing method is known as fused deposition modeling (FDM). This technique involves the melting of a solid strand of material through a heated and motor-driven nozzle before each layer solidifies on the build platform to create a 3D solid. The resolution is governed by the diameter of the extrusion nozzle. The solidification of individual layers immediately after extrusion leads to poor mechanical performance of parts as there is a weak connection between each layer [31]. FDM commonly utilizes thermoplastic material spools such as acrylonitrile butadiene styrene (ABS) and polylactic acid (PLA). Copper and iron particles of less than 43  $\mu\text{m}$  diameter have been successfully implemented into ABS for use as FDM filament [33]. The composite showed a decrease in mechanical strength and only a slight increase in thermal conductivity; both can be attributed to the direct relation between the particle loading and number of voids [33]. Since PDMS is a thermoset polymer that initially uses heat to cross-link and cure in an irreversible chemical reaction, it cannot be melted again or used directly in an FDM process. However, PDMS microfluidic devices with a minimum channel diameter of 90  $\mu\text{m}$  have been produced using an FDM produced ABS scaffolding that is dissolved away with acetone after curing the PDMS [34].

### **2.1.2 Conformal**

Conformal 3D printing is an extrusion technique in which a fluidic material is deposited onto a supporting solid reverse molded surface. The resolution is determined from the minimum movement distance of both the dispenser as well as the build stage [35]. The supporting structure allows complex geometric shapes such as a helix coil or screw [35]. PDMS has been successfully printed using a conformal support substrate of Carbopol, which acts as a reverse mold, to create

linear, helical, and bifurcation geometries [36]. Conformal processes have the advantage of not requiring stability of the printed material until after curing due to the complete support of the conformal surface. This process has the disadvantage of requiring the design of a second material to form the mold.

### **2.1.3 Stereolithography**

Stereolithography involves curing by cross linking of photoresin polymers or photoinitiator additives typically by UV or visible light and is proven for production of polymer nanocomposites [37]. A light source directed by mirrors into a bath of photoresin cures the surface layer as the build plate gradually pulls the part away from the surface. The resolution of these light curing techniques currently is around 100 nm with resolutions of tens of nanometers predicted for the near future as the spot size of lasers reduces and the absorption spectra of photoresins is further optimized [31], [35]. Micro-stereo lithography has been used to create intricate PDMS lab-on-a-chip devices with resolutions of 50  $\mu\text{m}$  [38]. The further improved process of digital light processing in which an entire layer of resin is cured by a liquid crystal display is implemented to create complex lab-on-a-chip shapes with a 3D printed mold that supports the desired PDMS structure and is dissolved away after curing [39]. However, the photopolymers used for stereolithography are not well suited for the addition of materials, as the radiative properties of these compounds must be very specific to ensure high resolutions during the light curing process [40].

### **2.1.4 Direct Ink Writing**

Direct ink writing (DIW) consists of extrusion through a nozzle of rheologically tailored inks with shear thinning behavior, which allows for shape retention following deposition. DIW comprises a variety of methods including robocasting, micropen writing, and droplet based approaches like inkjet printing and hot-melt printing [41]. The materials used for these inks include colloidal suspensions, colloidal gels, waxes, and melted polymers [41]. DIW involves inducing flow of a viscoelastic gel-like material by exceeding the yield stress to force the material through the nozzle. The sample quickly regains its solid-like behavior and maintains its printed shape in the absence of additional shear stress [40]. The DIW technique has been successfully used to create epoxy filled with graphene nanoplatelets and carbon nanotubes for

thermal management devices [42]. A three-phase PDMS ink consisting of precured PDMS microbeads, uncured PDMS liquid precursor, and water was developed with a high elastic modulus and yield stress capable of DIW with fast 3D printing in the vertical direction due to its shape retention [43]. A two component PDMS ink consisting of high viscosity DOWSIL SE-1700 and low viscosity Dow Corning Sylgard 184 at 85 wt. % and 15 wt. %, respectively, were combined for DIW of elastic strain trapping structures [44]. The inks were deposited through a Nordson EFD nozzle onto an Aerotech 3D positioning stage with pressure control from a Nordson EFD Ultimius V pressure box before being heat cured after printing at 100 °C for 30 minutes to fully solidify the PDMS [44].

Ozbolat et al. further refined this two-component PDMS mixture by optimizing the printing parameters of inks with a 7:3, 8:2, and 9:1 SE 1700: Sylgard 184 ratios [45]. The printing setup included an INKREDIBLE 3D bioprinter with Nordson EFD tips and Nordson EFD Ultimius V high precision dispenser extrusion pressure control [45]. The printing parameters that varied includes 410-610  $\mu\text{m}$  tip diameters, 150-300 kPa extrusion pressures, and 30-300 mm/min printing speeds [45]. The rheological characteristics over a range of PDMS ratios were analyzed for both shear rate and frequency dependence all of which aided in assessing the printability of the PDMS ink [45]. The setup was able to print complex biological structures such as a hand, nose, and blood vessel with increased mechanical and cell adhesion properties when compared with a cast sample [45].

We selected the DIW approach refined by Ozbolat et al. for creating a PDMS TIM. DIW does not require a molded material, offers a broad array of material selection including easy addition of nanoparticles due to the rheological control of the polymer base, and has been proven to be successfully printable through a range of viscosity values with modification to the printing parameters.

## **2.2 Graphene Nanoplatelet Particle Selection**

From the selection of DIW as our 3D printing method, specific rheological requirements are established for the design of the composite material. The goal of the TIM nanocomposite shape selection is to have the lowest enhancement of viscosity for the specific particle type so that a larger quantity of nanoparticles can be added. This will in turn provide the highest thermal conductivity values. This design approach differs from previous TIM designs in which only

thermal conductivity is considered as molded processing approaches do not have to control viscosity as precisely for composite production. Thus, the nanoparticle shape that has the least enhancement to viscosity at an equal particle loading is desired.

We must understand the effect of particle shape on viscosity to design for this objective. Experimental data for ZnO nanofluids showed a 7.7% and 5.9 % greater viscosity enhancement for rectangular particles over spherical particles at equal 0.5 vol. % to 5.0 vol. % [46]. This difference was attributed to the larger aggregate sizes seen for rectangular particles [46]. SiO<sub>2</sub>-H<sub>2</sub>O and Al<sub>2</sub>O<sub>3</sub>-H<sub>2</sub>O experimental data was used to create a modified Krieger and Dougherty model that accounted for the eccentricity of prolate spheroids [47]. The model showed that the viscosity significantly increases with increase in the effective radii of aggregates as well as with increased eccentricity [47]. This trend was explained for simulations of magmatic flows as the maximum packing fraction,  $\phi_m$ , is highest for spherical particles that can most efficiently pack and decreases for particles of increased eccentricity, meaning spherical particles would have the lowest viscosity at the same loading [48]. However, from comparison of the rheological characteristics of carbon-based nanomaterials including cylindrical carbon nanotubes, spherical buckyballs, sheets of graphene, x-shaped junctions, and y-shaped junctions, the particle shape that showed the lowest viscosity enhancement was graphene sheets [49], [50]. Molecular dynamics simulations that compared icosahedral, rod, and sheet particles at 5 vol. % concluded that sheets had the lowest viscosity enhancement [51]. The physical phenomenon that caused this trend was that the polymer chains appeared to intercalate between the sheets to lower direct particle contact. This effect caused the sheets to show much less bridging, where two or more nanoparticles were in direct contact, than the other shapes, which was also established as the largest contributor to the viscosity of the nanocomposites [51]. Experimental data for alumina nanofluids again confirms that sheet, or bladed, shape particles give the lowest viscosity increase at equal concentrations compared to brick, cylinder, and platelet values [52].

Therefore, the optimal particle shape for the design of a TIM in terms of viscosity is sheet-like particles. Graphene is the most popular material in the shape of sheets, and its superior thermal characteristics, especially in the in-plane direction, are very well documented [53]. Graphene should also increase the shear thinning behavior of the base polymer, which is desired for 3D printing via DIW, as is seen for a Newtonian glycerol base fluid becoming shear-thinning from the addition of graphene sheets [54]. Since graphene's sheet-like structure should have

excellent rheological properties, the remaining factor for particle selection is to have the largest enhancement to thermal conductivity. A comparison between the viscosity and thermal conductivity of graphene nanoplatelets (GNP) with different specific surface areas of 300, 500, and 750 m<sup>2</sup>/g showed similar viscosity values with the thermal conductivity directly related to the specific surface area [55]. The highest thermal conductivity enhancement was 27.64 % for the 750 m<sup>2</sup>/g GNP at only 0.1 wt. % loading [55]. Single-layer graphene sheets may show even less viscosity enhancement compared with GNP, but the GNP's are only several nanometers, or several graphene layers thick, while also being much more cost effective than the single-layer sheets. As a result, the GNPs with a specific surface area of 750 m<sup>2</sup>/g were selected as the TIM filler.

### 2.3 Sample Preparation

The production of PDMS-GNP samples followed a very similar procedure to that of previous literature for pure PDMS [44], [45]. The higher viscosity PDMS component is DOWSIL SE 1700 translucent adhesive from Dow Chemical. SE 1700 is a two-part, non-flowing, and heat curable PDMS for sealing printed circuit board components and bonding PC key pads. The lower viscosity PDMS component is Sylgard 184 silicone elastomer from Dow Chemical which is a clear two-component, flowing, and heat curable PDMS that is one of the most common formulations. Both components require weighing out a 10:1 ratio of polymer base to curing agent. The two base components are combined at different weight ratios to achieve the desired rheological properties for DIW. If filler is included, GNPs are then weighed out and added based on the weight of the overall PDMS mixture and the required weight percent of GNPs. The GNPs used for testing have a specific surface area of 750 m<sup>2</sup>/g and are obtainable from Sigma-Aldrich.

Samples are thoroughly mixed in a FlackTek DAC 400.1 FVZ SpeedMixer, which is a dual asymmetric centrifuge with mixing speeds from 800-2750 rpm. Samples with lower concentrations of GNP were mixed with two 30 second cycles at 2000 rpm with a 30 second rest period between the cycles. For the higher GNP loadings, the mixing speed was increased to 2500 rpm for complete dispersion of particles throughout the PDMS base. The rest periods were essential as the centrifugal mixing causes frictional molecular heating of the sample and any increases in temperature will cure the sample at a faster rate and increase the viscosity. No

further modifications are made before viscosity testing. Thermal conductivity testing requires cured solid samples so an Across International vacuum oven is utilized. The oven first degasses the samples at room temperature with 29-30 mmHg vacuum pressure before curing the pure PDMS samples at 80 °C for two hours. Addition of GNPs hinders the curing process so higher curing temperatures and longer times are required.

## 2.4 Viscosity Measurement Technique

Rheological characterization is conducted on a cone and plate rheometer. The specific rheometer model is a Malvern Bohlin Gemni 200 HR Nano. The device has no temperature control but records temperatures during testing, and only a 1-2 °C difference was observed. All tests were done at room temperature from 21-23 °C, which matches the conditions for DIW printing. The cone was 40 mm in diameter and angled at 4 ° with a 150 mm gap size between the cone and plate. Viscosity is determined with a small angle approximation, the physical constants of the system, and input torque of the device as

$$\mu = \frac{3T\theta}{2\pi R^3\omega}, \quad 25$$

where  $T$  is the total torque,  $\theta$  is the angle of the cone,  $R$  is the radius of the cone, and  $\omega$  is the angular velocity. The shear rate is defined as  $\dot{\gamma} = \frac{\omega}{\theta}$ . The device operates by inputting a torque to the system while using encoders to read the angular velocity of the cone at the given torque to then calculate the fluid's viscosity using Equation (25). The torque resolution is better than 1 nNm and the position resolution is 50 nano radians. Uncertainty propagation of Equation (25) showed that the torque resolution has the greatest impact on the viscosity uncertainty at low shear rate and that viscosity uncertainty will be lower at higher shear rate due to their inverse relation. Uncertainty should also be higher at lower shear rates due to the increased possibility of slip.

## 2.5 Experimental Viscosity of PDMS with GNP

Experimental viscosity measurements with the rheometer start with tests of pure PDMS without any GNP filler. These tests are used to validate the current setup and confirm the printable viscosity range that was established and optimized in literature [45]. The tests began with samples of the single PDMS compounds of SE 1700 and Sylgard 184 individually before

mixing them together and testing their viscosity at different weight ratios as is seen in Fig. 3. The first number of the PDMS ratio is always the high viscosity component SE 1700 and the second number is the low viscosity component Sylgard 184.

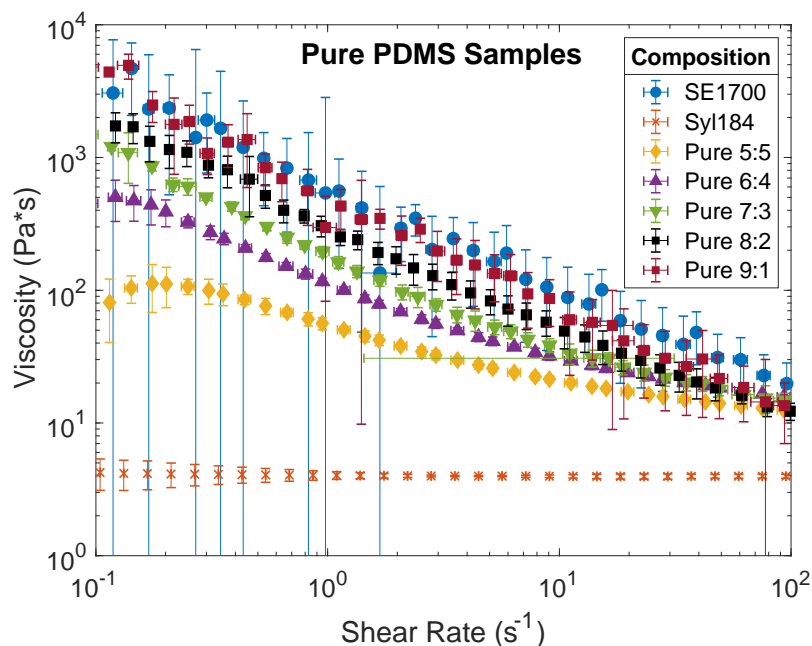


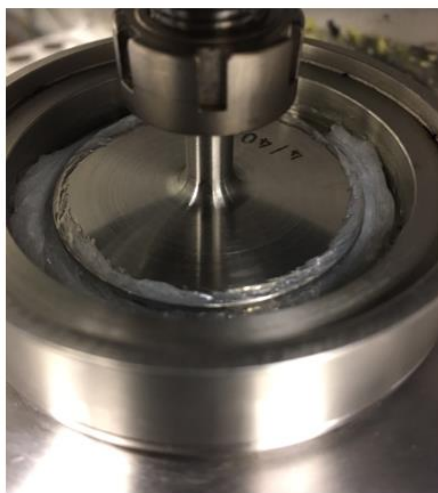
Figure 3: The measured viscosity as a function of the shear rate for each PDMS component and the mixed weight ratios of SE 1700: Sylgard 184.

Figure 3 shows that the low viscosity Sylgard 184 is Newtonian and gives a constant viscosity value throughout the shear rates that are tested. SE 1700 demonstrates relatively constant shear-thinning behavior from 0.1 to 100  $\text{s}^{-1}$ . When mixed together, the Sylgard 184 lowers the viscosity of the mixture with a larger effect at higher weight ratios. However, the rheological profile of the mixture still maintains much of the shear-thinning characteristics of pure SE 1700, shifted downward due to the additional lower viscosity component. The 5:5 PDMS ratio shows a more drastic decrease to the viscosity than any other PDMS ratio tested. This effect is likely caused by decreased entanglement of the SE 1700 chains, which are longer than the Sylgard 184 chains. The shear thickening seen in the 5:5 PDMS ratio composition at very low shear rate is likely an effect of the sample not yet reaching steady state and error arising from the measurement technique as it calculates for steady shear flow [56].

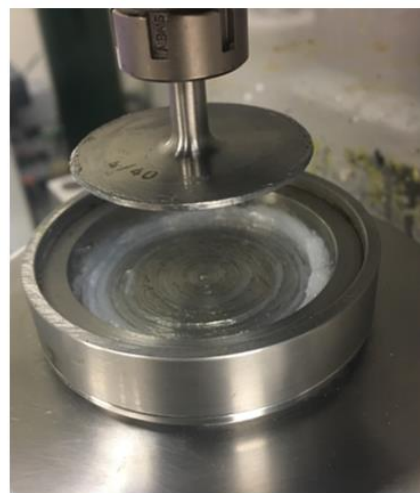
Since the device inputs a torque that tries to match a desired shear rate, there is uncertainty with both the shear rate and measured viscosity of each data point. The shear rate

uncertainty was largest at low shear rates due to a limited torque resolution. Therefore, multiple tests (at least 3) of each composition were performed for the full shear rate range to reduce uncertainty. To group data from multiple tests with unequal shear rates, the measured values were placed into bins based on the closest target shear rate on a logarithmic scale. The points in the figure are located at the average value for each of the bins. The statistical uncertainty for all experimental data is found and plotted from a Student's t-distribution, which accounts for the number of measurements taken and standard deviation of each group point. A student's t-distribution is valid for data with less than 30 measurements. A larger number of tests is completed for the pure PDMS mixtures due to these values establishing the base fluid viscosity without filler, which appears in all viscosity models from literature. The Student's t-distribution for uncertainty is symmetric about the data point in Cartesian coordinates; however, the uncertainty appears larger below the data point in the figures due to the plots being log-log scale.

A moderately consistent trend in the data was larger uncertainty in mixtures that had a higher concentration of SE 1700. This increased uncertainty is primarily caused by the increased viscoelastic effects of SE 1700 that allow it to be used for 3D printing by DIW. As seen in Fig. 4a., the sample rises to the top of the cone, similar to the Weissenberg effect for rotating rods. Fig. 4b. shows that after several measurements the sample gradually collects on the edges of the plate outside of contact with the cone. Both effects lead to a loss of accuracy in the measurement because the calculations assume complete contact between the fluid and the cone and plate.



a.) After 1<sup>st</sup> measurement



b.) Post measurements

Figure 4: Viscoelastic effects of SE 1700 give rise to a larger uncertainty in the results.

The strong viscoelastic properties are not seen when testing the Sylgard 184. As is evident from Fig. 5, the more fluidic characteristics of Sylgard 184 lead to its lower uncertainty during testing. The sample neither creeps to the top of the cone or overly spreads, in stark contrast to the SE 1700, allowing for more complete contact between the fluid and the rheometer. These effects are the primary reason why SE 1700 and mixtures with a higher concentration of SE 1700 generally show higher uncertainties in the viscosity results. Originally,  $10^{-2}$  through  $10^3 \text{ s}^{-1}$  shear rates were to be tested, but this range was reduced to  $10^{-1}$  through  $10^2$ . The low shear rate bound was increased due to the large uncertainties caused by the limited torque resolution of the device, slip between the fluid and device, and non-equilibrium of the fluid before it reaches steady state. The high shear rate bound was decreased due to the SE 1700's viscoelastic effects that removed nearly all of the sample from under the cone particularly at very high shear rates.



a.) After 1<sup>st</sup> measurement



b.) Post measurements

Figure 5: Cleaner data for Sylgard 184 is due to its more fluidic properties.

Figures 6 – 10 show the viscosity of different ratios of PDMS with the addition of GNPs. Figure 6 gives the lowest concentration of GNP filler, and much of the PDMS ratios look very similar to the pure PDMS without the addition of any filler. The 9:1 PDMS ratio is not included in filler testing as it was the upper limit of the printable viscosity range and significant filler addition will further increase viscosity requiring even higher extrusion pressures and further

processing difficulties. Further details of the effects at the lowest particle loadings are clearer when graphing the relative viscosity data in section 2.6.

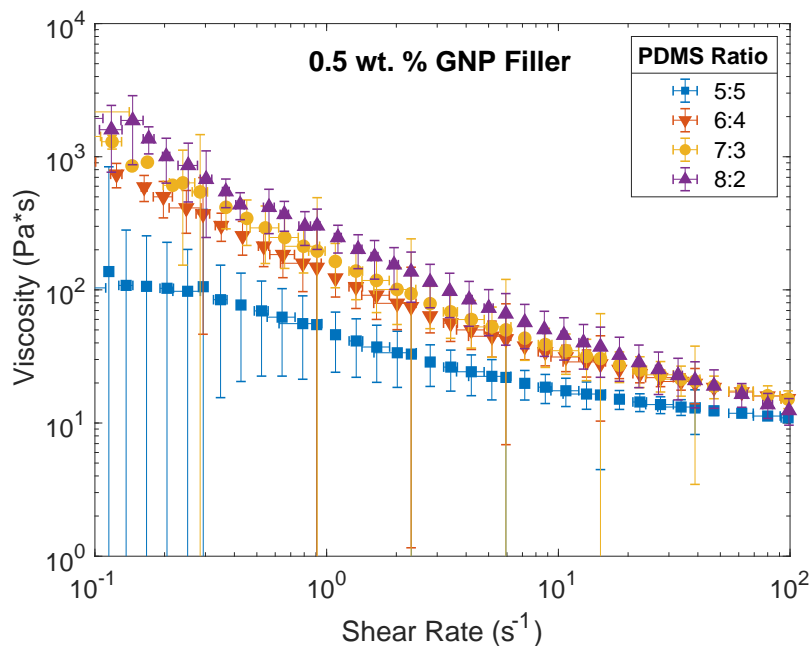


Figure 6: The measured viscosity as a function of shear rate for the lowest tested concentration of GNP filler at different PDMS ratios.

Comparable results are achieved in Fig. 7, which has a 0.5 wt. % increase in filler with respect to Fig. 6. The similar viscosities demonstrate that at the high base polymer viscosities associated with DIW 3D printing, the addition of a small amount of filler will not cause any drastic changes in the measured values. One point in the 8:2 PDMS ratio curve does not have uncertainty because it is the only data point for this shear rate range. One interesting phenomenon is that at the highest shear rates all the PDMS ratios coalesce into a very similar range of values. This effect is seen in the pure PDMS samples, but also with the 5:5 sample that has a much lower viscosity at low shear rates. This could be due to the increased concentration of Sylgard 184 with Newtonian behavior that keeps a constant viscosity with shear rate when compared with the strongly shear-thinning SE 1700.

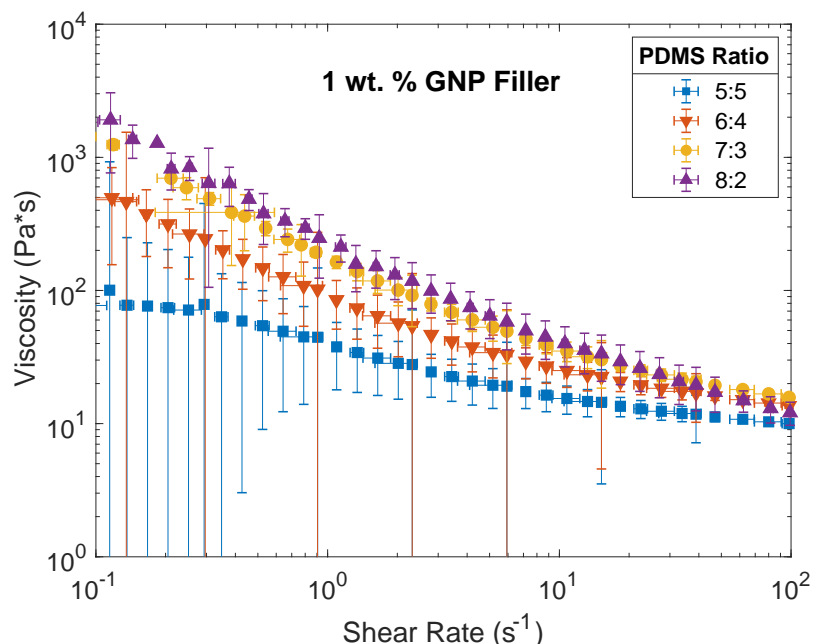


Figure 7: The measured viscosity as a function of shear rate for low GNP filler loadings at different PDMS ratios.

Noticeable change in viscosity is shown at 2.5 wt. % GNP filler at different ratios of PDMS concentrations in Fig. 8. The 2.5 wt. % GNP filler is nearing the limit of isolated filler concentrations. The results show a slight increase in viscosity for the 8:2 ratio PDMS, but interestingly also show a decrease in viscosity for the 5:5 ratio and little to no effect on the 6:4 ratio. This lubricating effect is not uncommon for nanoparticles and can be explained by the “ball bearing” effect [57]. This effect occurs when the shear rate between the narrow gaps that separate particles becomes exceptionally high and causes polymer chains to disentangle thereby reducing viscosity [58]. Figure 9 shows the viscosity results for a GNP loading of 5 wt. % at several different PDMS ratios. The results look very similar to Fig. 8 even though the number of GNPs has doubled. In Fig. 8 and Fig. 9, the increased particle loadings do appear to separate the viscosity values at high shear rates.

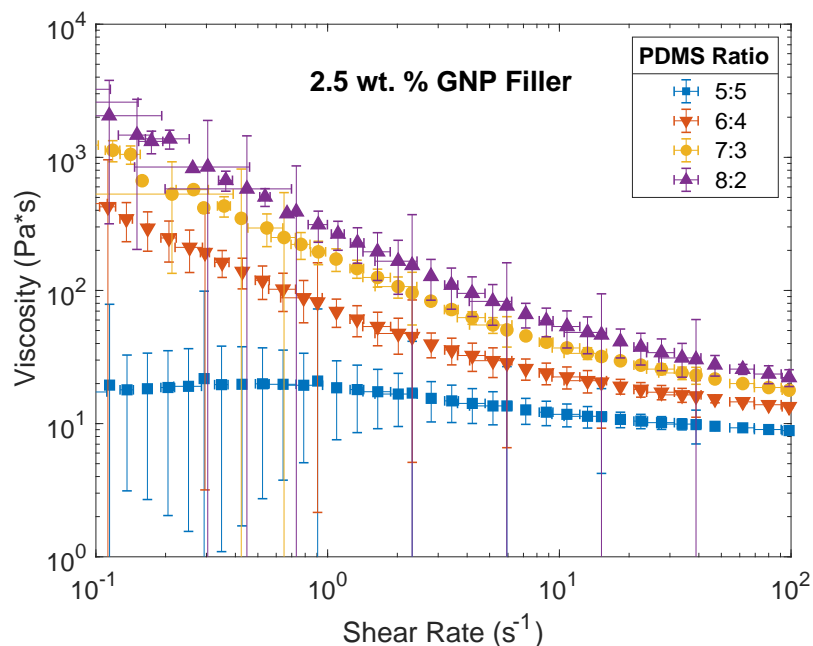


Figure 8: The measured viscosity as a function of shear rate for 2.5 wt. % GNP loading at different PDMS ratios.

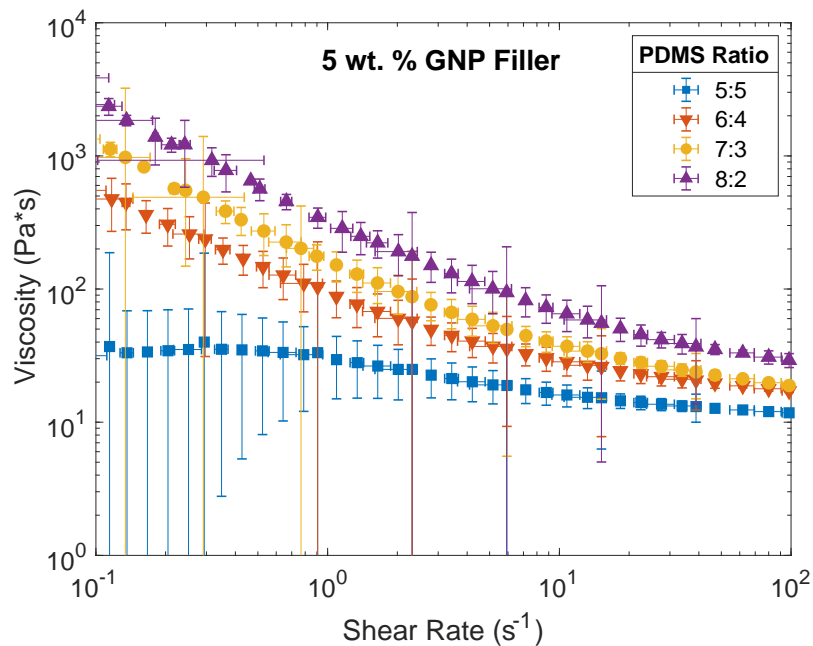


Figure 9: The measured viscosity as a function of shear rate for a moderate graphene loading of 5 wt. % at different PDMS ratios.

Figure 10 illustrates the effect of the highest particle loadings of GNPs on each of the tested PDMS ratios. At these high particle loadings, the viscosity becomes increasingly enhanced as the particles are no longer isolated and instead form clusters which increase in size at higher and higher loadings. The particles appear to affect the 8:2 and 7:3 PDMS ratios similarly as the curves are offset by comparable amount in each test before reaching about the same value at the highest shear rates. The 5:5 PDMS ratio sample shows even greater enhancement as its viscosity values overlap with the 6:4 ratio in Fig. 10b. at 15 wt. % GNP and similarly, the 6:4 PDMS ratio overlays the 7:3 ratio sample in Fig. 10c. at 20 wt. % GNP. These results are a consequence of the filler particles dominating the viscosity behavior at very high particle loadings and concealing much of the base fluid effects. The 15 wt. % GNP and 20 wt.% GNP in Fig. 10b. and Fig. 10c. respectively showed strong viscoelastic effects during testing analogous to the pure SE 1700 making it difficult to obtain accurate measurements so these PDMS and GNP compositions are likely near the upper limit to the testable viscosity range for the current rheometer setup.

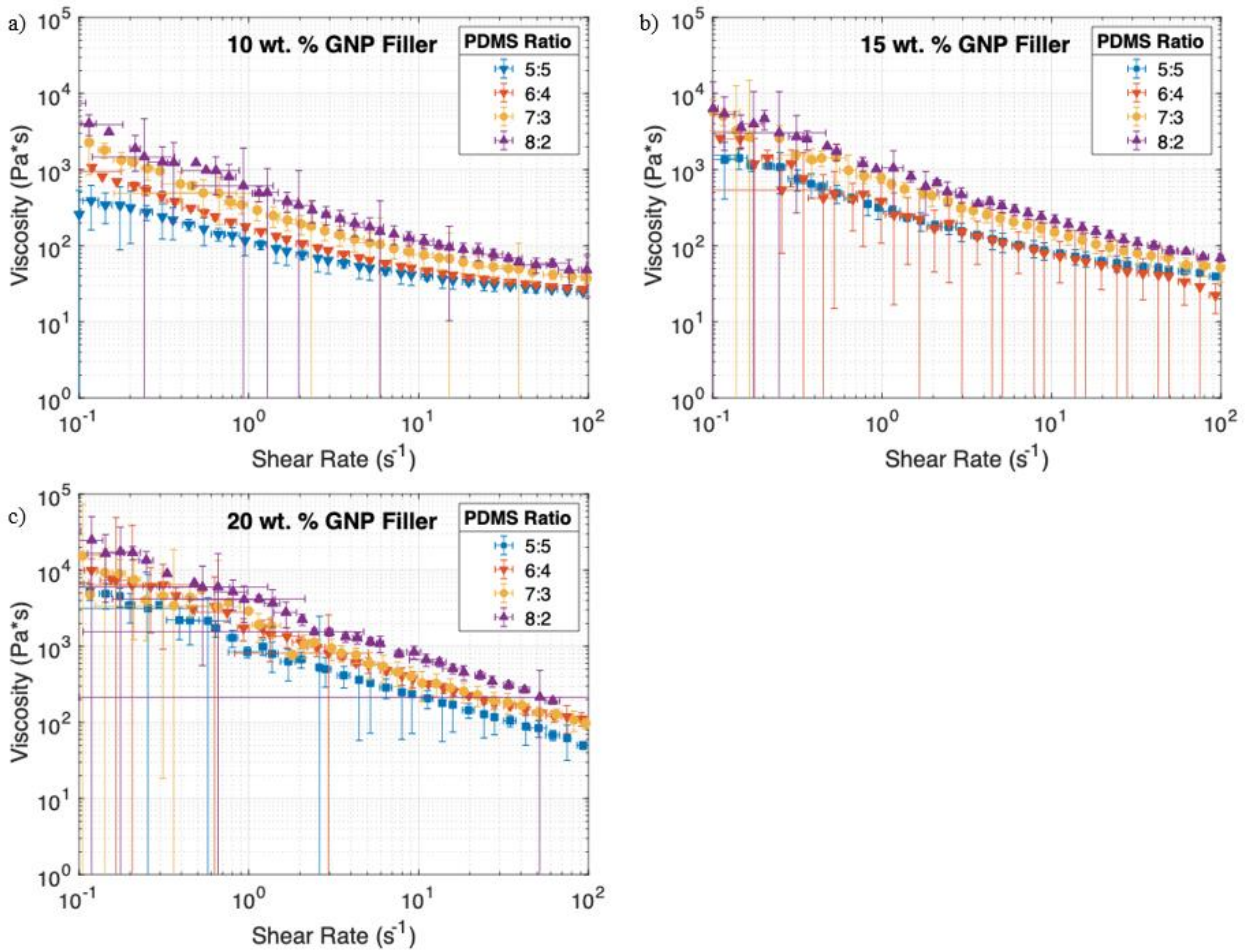


Figure 10: The measured viscosity as a function of shear rate for the highest tested GNP loadings.

## 2.6 Modeling of Viscosity

Now that complete viscosity data from  $10^{-1}$  to  $10^2 s^{-1}$  shear rates is available, the viscosity models from literature are used to fit to the experimental data. Models are fit for the 5:5, 6:4, 7:3, and 8:2 PDMS ratios from 0 to 20 wt. % GNP loading which is converted to vol. %,  $\phi$ , to agree with the models. This procedure is completed for shear rates of 10 and  $60 s^{-1}$  which correspond to the values in which the lowest uncertainties are seen for all measurements. Analysis of a range of shear rates is important because each value corresponds to a different printing speed for processing. Also it has been shown that differences in rheological findings from literature can often be accounted by the distinct nature of fluids at different shear rates [59]. In fact, particle and polymer chain alignment that gives the shear thinning behavior from shear rates of  $10^{-1}$  to  $10^2 s^{-1}$  in our work is only a part of the nanofluid behavior. The Newtonian plateau at higher

shear rates is observed once no more alignment can occur, and if even higher shear rates are tested a shear thickening region will develop as particle clusters are destroyed and particles disperse randomly before the alignment process once again occurs leading to shear thinning effects [59]. Each model from literature fit to the experimental data is outlined mathematically in section 1.2.3 and its subsequent subsections. The second order constant in Batchelor's model as well as the  $\phi_{ma}$  and  $\phi_m$  parameters from Chen's model were fit using the MATLAB function `lsqnonlin`, which is a nonlinear least squared approximation.

An accurate intrinsic viscosity value must be obtained as it is a common parameter for all the viscosity models from literature. The intrinsic viscosity describes the effect of gradually adding filler to a composite material on viscosity when the filler particles are sufficiently large compared with the matrix particles. The Huggins and Kraemer multi-point fit equations correspond to the limit as the concentration approaches zero for the reduced viscosity,  $\eta_{red}$ , and inherent viscosity,  $\eta_{inh}$ , respectively. The Solomon-Ciuta single-point procedure from Equation (19) is also calculated for the two lowest concentrations of filler tested, which is shown as  $\eta_s$ . The Solomon-Ciuta equation is unable to account for the sign of intrinsic viscosity due to a square root in the equation; therefore, anytime the Huggins and Kraemer solutions were negative, a negative one was multiplied to the Solomon-Ciuta values. The intrinsic viscosity value obtained by the Huggins equation is used as an input to the models from literature due to generally showing the best fit value. The procedure for calculating the intrinsic viscosity is further described in section 1.2.2.

The viscosity results for the effect of filler on the 5:5 weight ratio PDMS at a shear rate of  $10 \text{ s}^{-1}$  is shown in Fig. 11 and Fig. 12. The Solomon-Ciuta values for intrinsic viscosity verify the multi-point fit procedures as they look to average out to be the Huggins multi-point fit value. The Huggins equation gives a value of -0.3316 and the Kraemer equation gives a value of -0.3815. The negative intrinsic viscosity physically implies that the filler has a lubricating effect, that was seen clearly in polycarbonate filled with glass beads, at low volume concentrations that lowers viscosity below that of the base PDMS [60]. This lubricating effect is seen most clearly in the 5:5 ratio PDMS samples as the viscosity of the base fluid is not recovered until after 5 wt. % GNP loading. This lubrication effect is very beneficial for nanofluid applications as there will be decreased pumping power accompanied by increased thermal conductivity which are usually mutually exclusive objectives.

Figure 12 shows that the Chen's model using both the maximum packing fraction of aggregates,  $\phi_{ma}$  and maximum packing fraction of particles,  $\phi_m$  gives the best fit for any model from literature. The model by Batchelor also has decent agreement, but overpredicts the viscosity at low loadings and underpredicts the value at the highest loading tested. The Einstein and KD classical models have fair agreement with the data until after 0.03 vol. concentration when particle interactions are insignificant. However, all models do not accurately describe the lubricating effect of the nanoparticles and therefore, overpredict the viscosity at low filler concentrations.

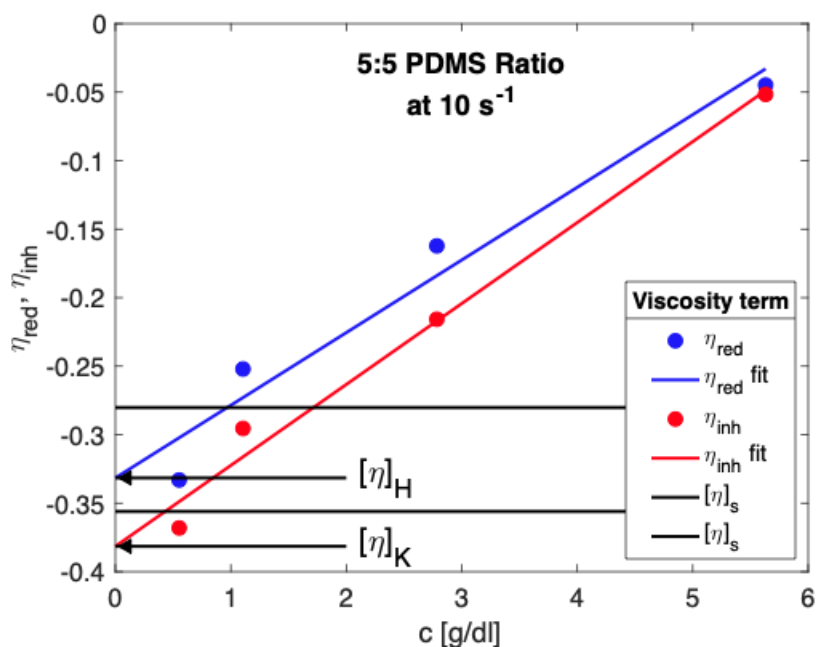


Figure 11: Intrinsic viscosity fitting for 5:5 PDMS ratio at a shear rate of  $10 \text{ s}^{-1}$ .

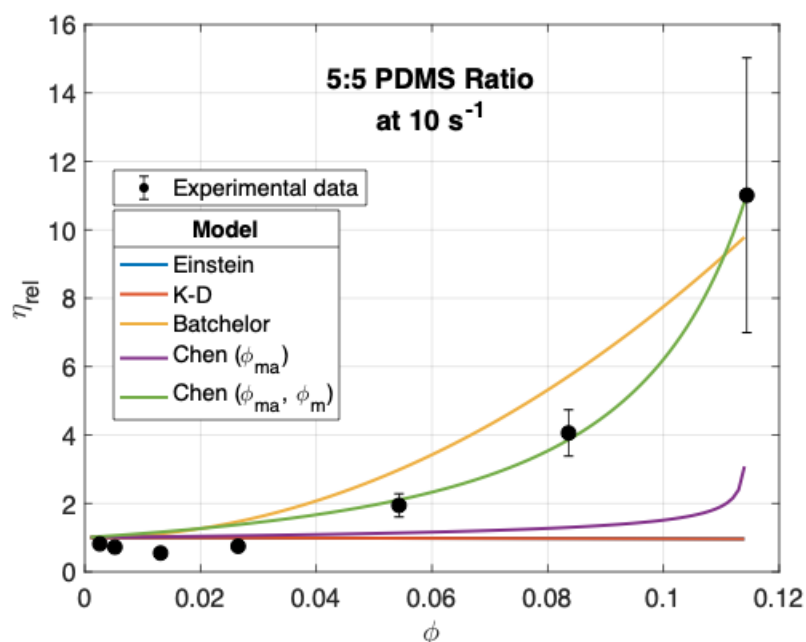


Figure 12: Viscosity model fitting to the experimental data of 5:5 PDMS ratio with GNP filler at a shear rate of 10 s<sup>-1</sup>.

The effects of adding GNP filler on the 5:5 PDMS ratio at an increased shear rate of 60 s<sup>-1</sup> is shown in Figs. 13 and 14. Figure 13 displays the intrinsic viscosity fitting. The Huggins equation corresponds to the lowest Solomon-Ciuta fit with a value of -0.2330 and the Kraemer equation gives a value of -0.2561. These values still indicate a lubricating effect, but not as strong as what is seen at a shear rate of 10 s<sup>-1</sup> for the same sample. Chen's model using two fit parameters once again gives a great fit to the experimental data. If Chen's model is fit only using the maximum packing fraction of aggregates,  $\phi_{ma}$  with a constant particle packing fraction,  $\phi_m$  of 0.6 is used to fit to the data then only agreement with the lowest particle loadings is seen. The single parameter fit Chen model is comparable to the fit from classical models. Batchelor's model still overestimates the viscosity at low particle loadings, but unlike 10 s<sup>-1</sup> has excellent agreement at vol. concentrations above 0.05 rivaling that of Chen's model.

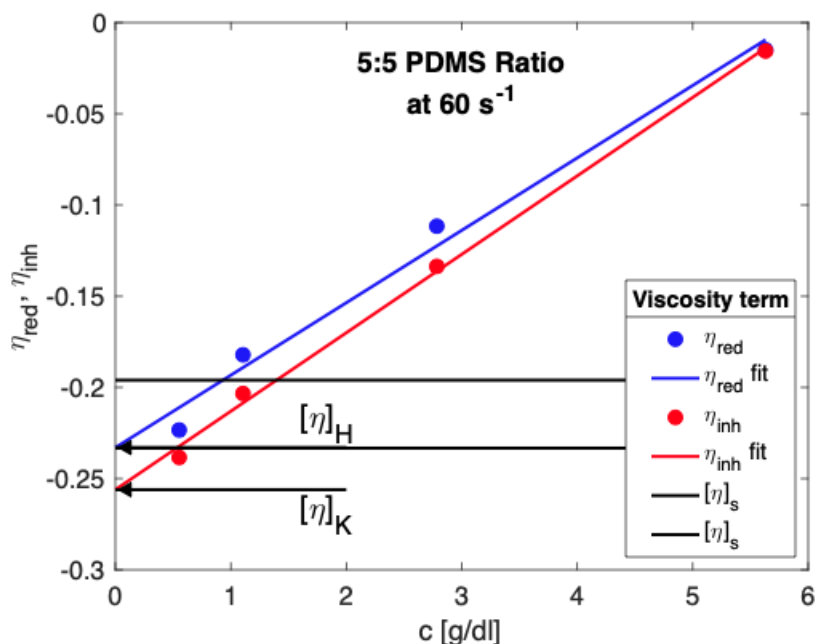


Figure 13: Intrinsic viscosity fitting for 5:5 PDMS ratio at a shear rate of 60 s<sup>-1</sup>.

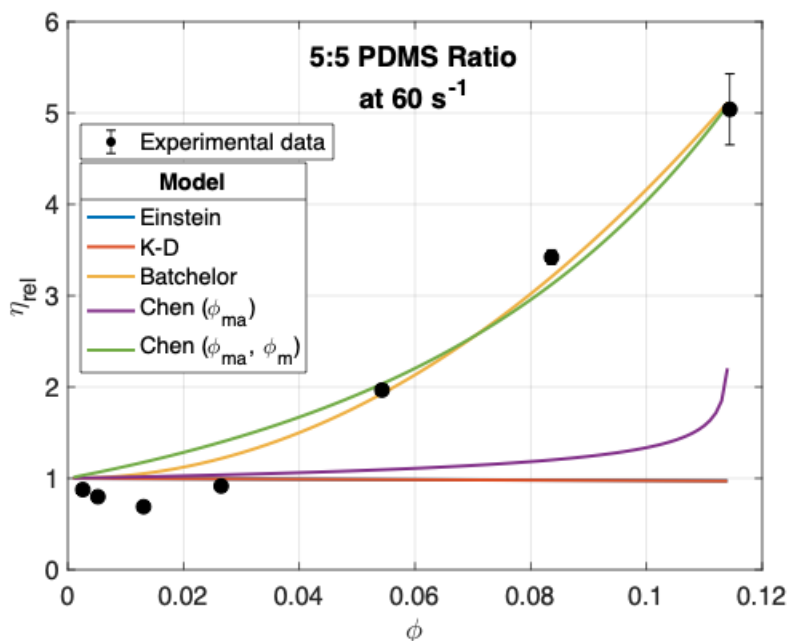


Figure 14: Viscosity model fitting to the experimental data of 5:5 PDMS ratio with GNP filler at a shear rate of 60 s<sup>-1</sup>.

Figure 15 gives the intrinsic viscosity for the 6:4 PDMS ratio at a shear rate of 10 s<sup>-1</sup>. The Huggins and Kraemer equations both appear to be about the average of the two Solomon-Ciuta

single-point fit procedures. The Huggins equation gives a value of -0.1354 and the Kraemer equation gives a value of -0.1518. Since a larger negative value means a stronger lubricating effect, the 6:4 ratio PDMS has less lubrication from filler compared with the 5:5 ratio PDMS at the same shear rate. The 6:4 ratio has about half the intrinsic viscosity of the 5:5 ratio. This trend is apparent in Fig. 16 at low concentrations as there is clearly a decrease in viscosity, but it is not nearly as drastic as that of the 5:5 ratio sample. Figure 16 also shows that the two fit parameter Chen model once again gives the best agreement. Batchelor's model has reasonable agreement with the highest particle loading, but greatly overpredicts the viscosity values before a vol. concentration of 0.10.

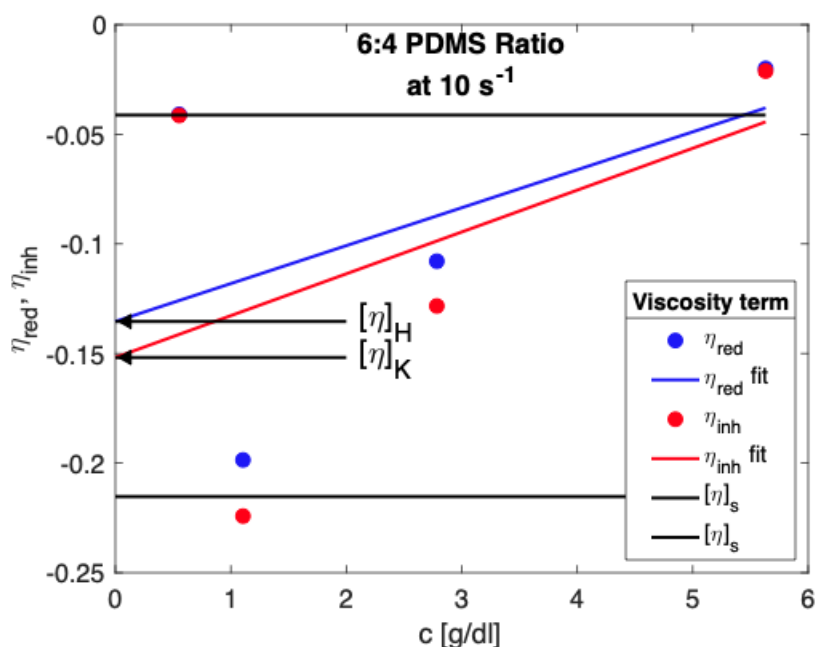


Figure 15: Intrinsic viscosity fitting for 6:4 PDMS ratio at a shear rate of  $10 \text{ s}^{-1}$ .

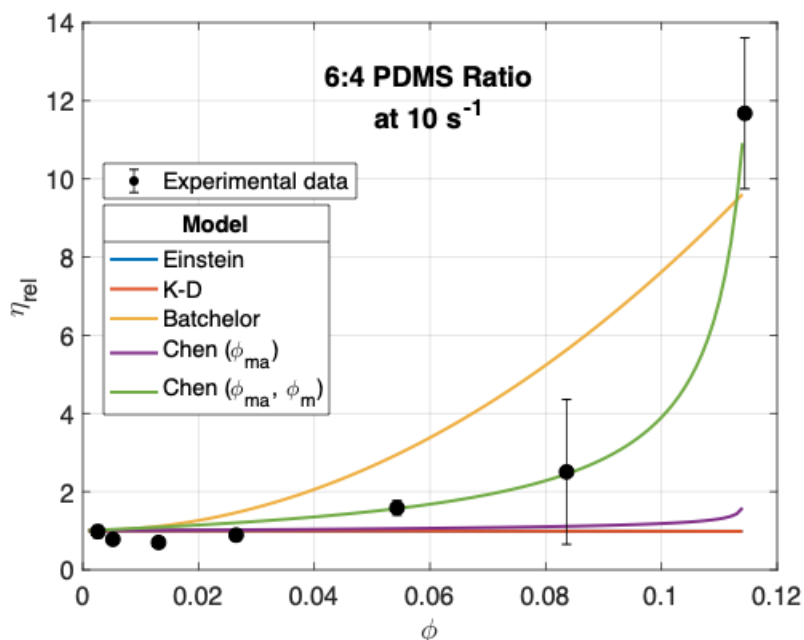


Figure 16: Viscosity model fitting to the experimental data of 6:4 PDMS ratio with GNP filler at a shear rate of  $10 \text{ s}^{-1}$ .

The experimental data for 6:4 ratio PDMS with GNP filler at a shear rate of  $60 \text{ s}^{-1}$  is shown in Figs. 17 and 18. The Huggins and Kraemer equations are nearly an average of the two Solomon-Ciuta values for intrinsic viscosity which is analogous to the 6:4 ratio PDMS at a shear rate of  $10 \text{ s}^{-1}$  in Fig. 15. The Huggins and Kraemer equations have values of  $-0.0944$  and  $-0.0998$  respectively. This follows the trend of the 5:5 PDMS ratio sample in that the higher shear rate has a lower lubricating effect. The overall viscosity enhancement from increased particle loading in Fig. 18 has a trend that is indistinguishable from the lower shear rate of  $10 \text{ s}^{-1}$ . This trend looks much different from the 5:5 sample as the viscosity begins to increase rapidly after a vol. concentration of  $0.09$ . Once again, the two parameter Chen model has excellent agreement with all experimental data while Batchelor's model matches the rudimentary trend.

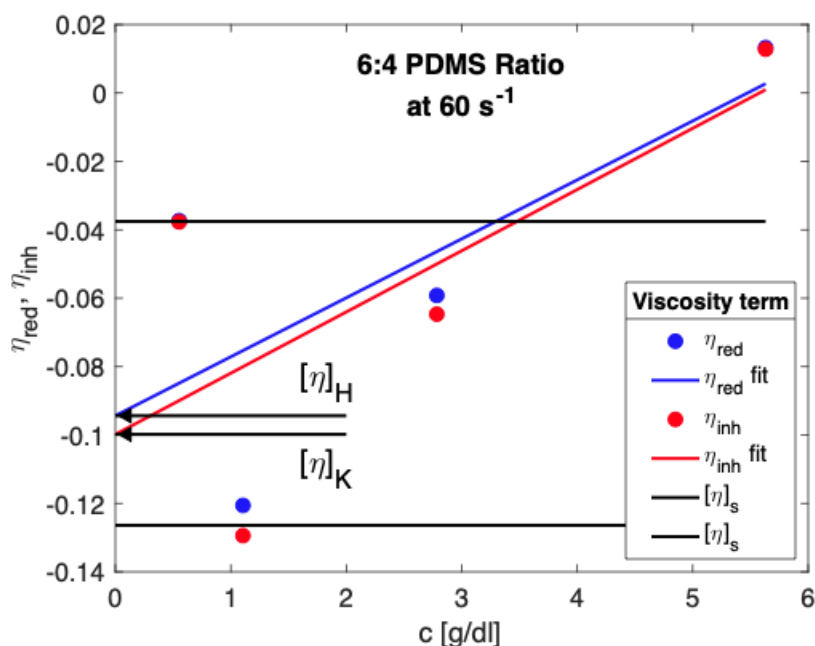


Figure 17: Intrinsic viscosity fitting for 6:4 PDMS ratio at a shear rate of  $60 \text{ s}^{-1}$ .

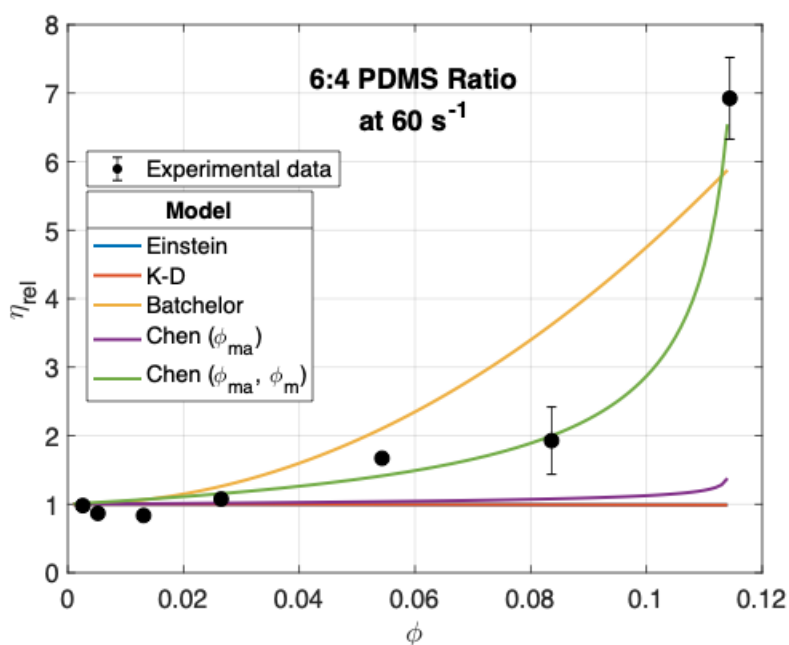


Figure 18: Viscosity model fitting to the experimental data of 6:4 PDMS ratio with GNP filler at a shear rate of  $60 \text{ s}^{-1}$ .

Figure 19 displays the values for intrinsic viscosity for 7:3 ratio PDMS at a constant shear rate of  $10 \text{ s}^{-1}$ . The Huggins equation gives an intrinsic viscosity of  $-0.1372$  and the Kraemer

equation gives an intrinsic viscosity of -0.1440. The lubricating effect is only noticeable for the lowest GNP concentration of 0.05 wt. %. The Einstein model fits the data well until  $\phi$  equals 0.02 to 0.03, as expected since Einstein's model does not account for any particle interactions that occur at higher vol. percent. Similarly, the KD model overlaps the Einstein model and does not characterize the values after particle interaction becomes significant. The two-parameter fitting of Chen's model once again shows very close agreement with the experimental data while Batchelor's model follows the general data trend without closely matching any one data point. All literature model fittings are seen in Fig. 20. The viscosity enhancement with filler vol. concentration is more gradual than the trend seen for the 6:4 PDMS ratio sample.

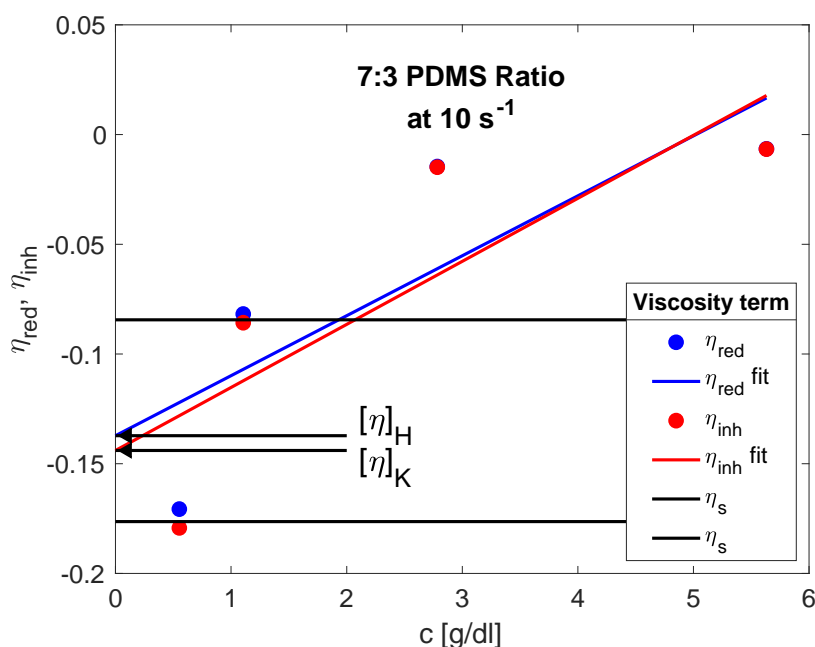


Figure 19: Intrinsic viscosity fitting for 7:3 PDMS ratio at a shear rate of  $10 \text{ s}^{-1}$ .

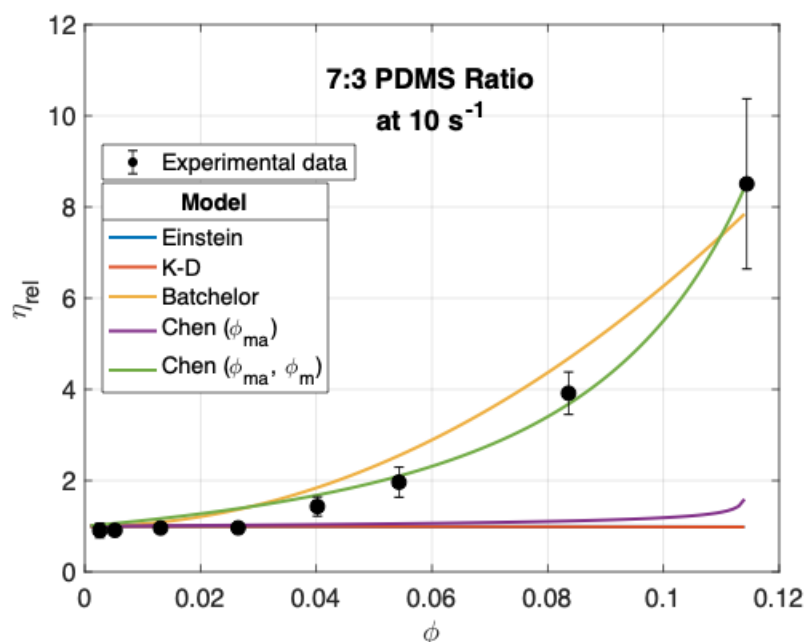


Figure 20: Viscosity model fitting to the experimental data of 7:3 PDMS ratio with GNP filler at a shear rate of 10 s<sup>-1</sup>.

The viscosity enhancement due to filler addition for the 7:3 PDMS ratio sample at a constant shear rate of 60 s<sup>-1</sup> is shown in Figs. 21 and 22. The general trend of increasing intrinsic viscosity with shear rate again holds. However, the positive intrinsic viscosity means that there is no lubricating effect even at very low GNP loadings as seen in Fig. 21. The Huggins and Kraemer equations give intrinsic viscosity values of 0.1095 and 0.1057, respectively. The viscosity enhancement is further illustrated in Fig. 22 as the relative viscosity has a value above one at all data points. This trend agrees well with Batchelor's model and does not appear to overpredict low concentration samples as seen in previous fittings. Chen's two-parameter fit model also has good agreement. Batchelor's model matches data from 0.04-0.06 vol. concentrations while Chen's model corresponds well to data at vol. concentrations of 0.08-0.10.

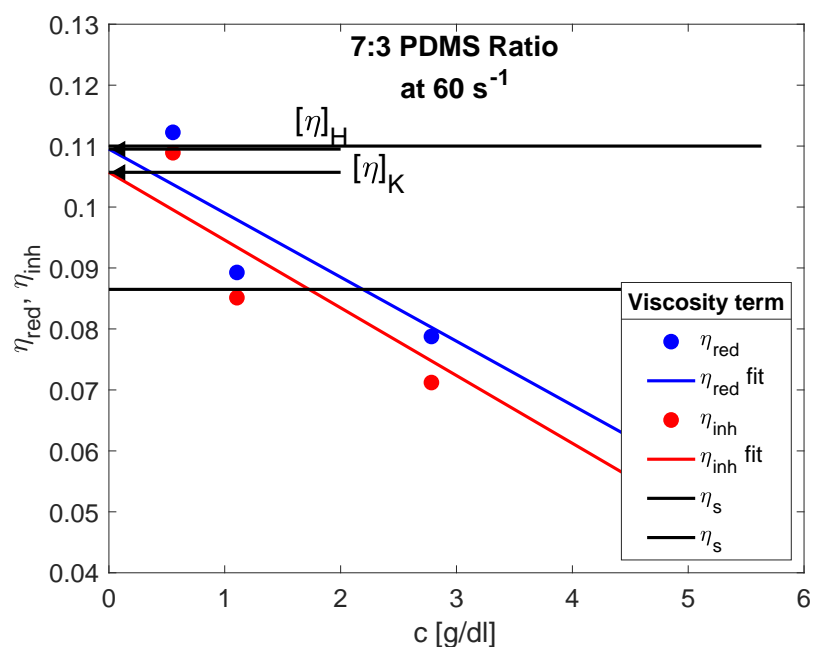


Figure 21: Intrinsic viscosity fitting for 7:3 ratio PDMS at a shear rate of 60 s<sup>-1</sup>.

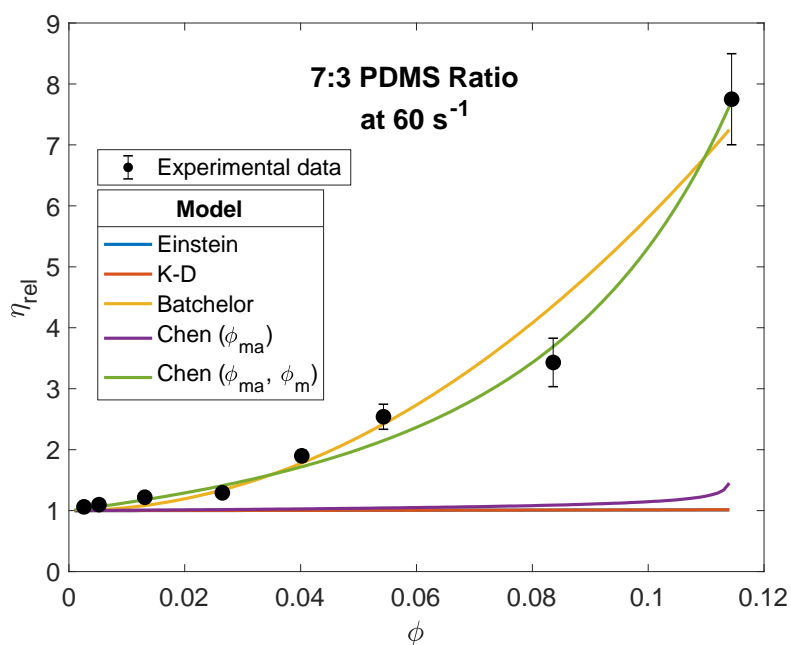


Figure 22: Viscosity models from literature fit to the experimental data for 7:3 ratio PDMS with GNP filler at a constant shear rate of 60 s<sup>-1</sup>.

At the lower shear rate of  $10 \text{ s}^{-1}$ , the 8:2 ratio PDMS in Fig. 23 shows a very similar intrinsic viscosity relation to the 7:3 ratio PDMS. The Huggins equation gives a value of  $-0.1637$  compared to  $-0.1372$  for the 7:3 ratio. Therefore, both PDMS ratios experience a lubricating effect at lower shear rates. This lubricating effect can be seen quite clearly in Fig. 24 for the 0.05 wt. % graphene which is the second data point. Again, the Einstein and KD models show good agreement up to 2 vol. %, and the Batchelor model agrees with the general trend of the data. The two-parameter fitting of Chen's model has outstanding agreement throughout the range of vol. concentrations and overlays all experimental data points.

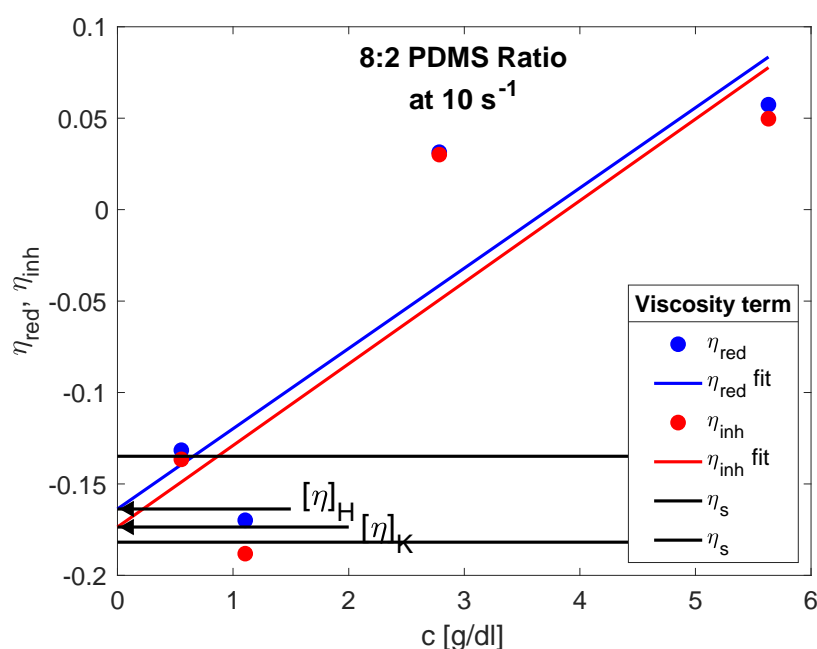


Figure 23: Intrinsic viscosity fitting for 8:2 ratio PDMS at a shear rate of  $10 \text{ s}^{-1}$ .

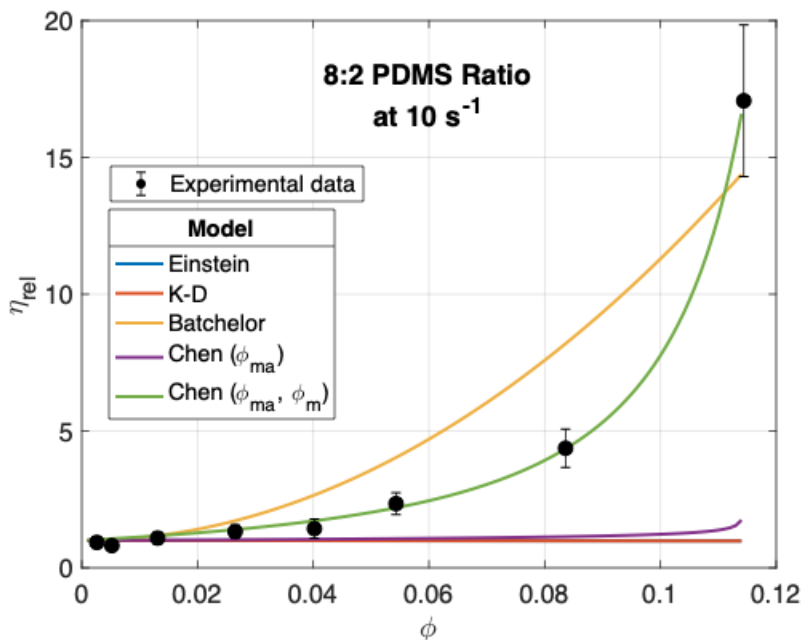


Figure 24: Viscosity models from literature fit to the experimental data for 8:2 ratio PDMS with GNP filler at a constant shear rate of  $10 \text{ s}^{-1}$ .

At a shear rate of  $60 \text{ s}^{-1}$  as seen in Fig. 25, the intrinsic viscosity for the Huggins equation is  $-0.0078$ , meaning that the particles have almost no effect on the viscosity at very low concentrations. The 8:2 ratio maintains a slight lubricating effect throughout the shear rate analysis likely due to the higher viscosity of the base polymer. The intrinsic viscosity of 8:2 ratio PDMS shows much of the same trends as the other PDMS ratios. Both polymer bases have a decrease in lubricating effect at higher shear rates described by the intrinsic viscosity, which increases with increasing shear rate. The classical models from literature have poor fitting with the experimental data except at less than 1 vol. %, as seen in Fig. 26. Unlike the lower shear rate of 8:2, the Batchelor model shows exceptional agreement with data except from 0.08 to 0.1 vol. concentrations. This overall enhancement trend is equivalent to the 7:3 PDMS ratio at the same shear rate and the Batchelor model fit both agree well. However, this is the only case in which the Chen model with two-parameter fitting does not have the best agreement with the data. Instead, both Chen fittings agree better with the classical models than the data or Batchelor's model. The reason for the lack of fitting is that the intrinsic viscosity of this sample and shear rate is almost an order of magnitude smaller than the other samples so the fitting procedure was unable to produce a viable model to match the data.

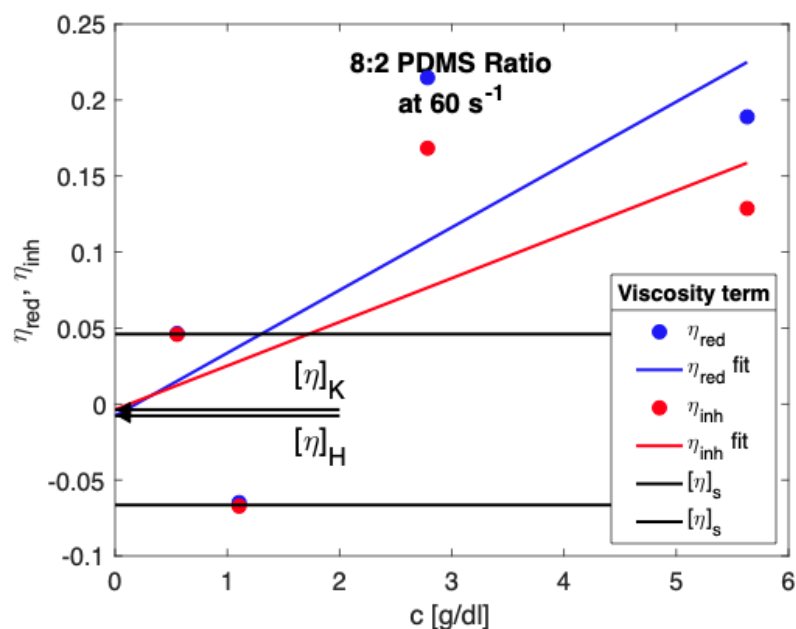


Figure 25: Intrinsic viscosity fit for a PDMS ratio of 8:2 at a shear rate of  $60 \text{ s}^{-1}$ .

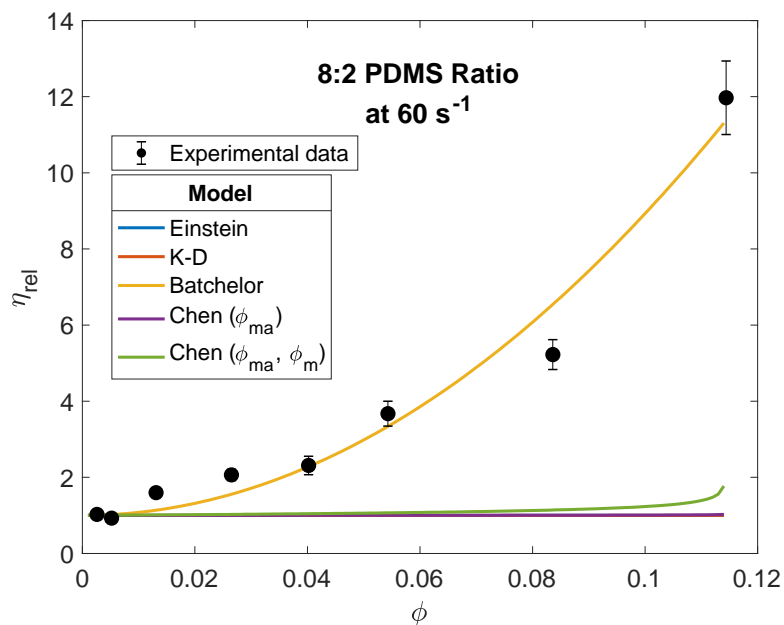


Figure 26: Viscosity model fitting of experimental data for 8:2 ratio PDMS with GNP filler at a constant shear rate of  $60 \text{ s}^{-1}$ .

One common trend for all samples was that the Einstein and KD classical models only showed good agreement up to 0.02 or 0.03 vol. concentrations. A closer look at the model fits at very low particle loadings for a 7:3 PDMS ratio at a constant shear rate of  $10 \text{ s}^{-1}$  is shown in Fig. 27. Clearly, the classical models show even better agreement than the Batchelor and Chen models which both overpredict the viscosity values at these low concentrations. The tradeoff is that the Batchelor and Chen models instead correspond to the data at higher vol. concentrations. However, none of the models from literature can precisely model the lubricating effects of the GNP filler at these low particle loadings.

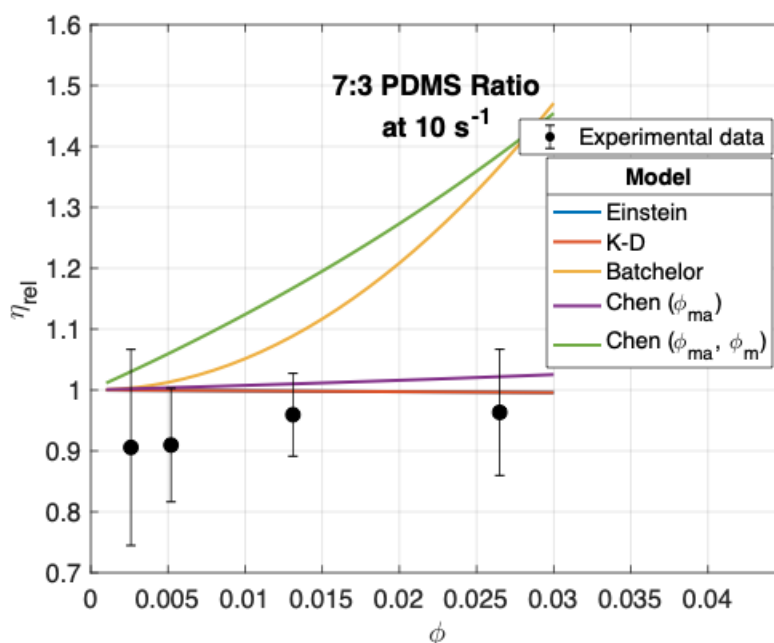


Figure 27: Viscosity model fitting of experimental data for low GNP concentrations of 7:3 ratio PDMS at a constant shear rate of  $10 \text{ s}^{-1}$ .

Another trend of model fitting seen in almost all of the tested samples is the discrepancy between using the one-parameter and two-parameter Chen model. As previously mentioned, the one-parameter model fits the experimental data to Chen's model using only the packing fraction of aggregates,  $\phi_{ma}$ , while the two-parameter fitting also includes the maximum packing fraction of particles,  $\phi_m$  which was at a fixed value of 0.6 for the one-parameter that corresponding to the maximum packing of spherical particles. The difference in these two fitting procedures is displayed in Fig. 28. While the two-parameter approach can effectively match the data, the values for both  $\phi_{ma}$  and  $\phi_m$  exhibit unphysical values. The two-parameter curve in Fig. 28 gives

a  $\phi_{ma}$  equal to 0.021 and a  $\phi_m$  equal to 14.185. The maximum packing fraction should give a value between 0.4 to 0.6 or at least from 0-1 to be physical. However, due to the much lower intrinsic viscosity values in these samples compared with the 2.5 used for spherical particles in Chen's model, the total exponent value closely matches the work of Chen, but gives a maximum packing fraction that is about an order of magnitude too large to be physical.

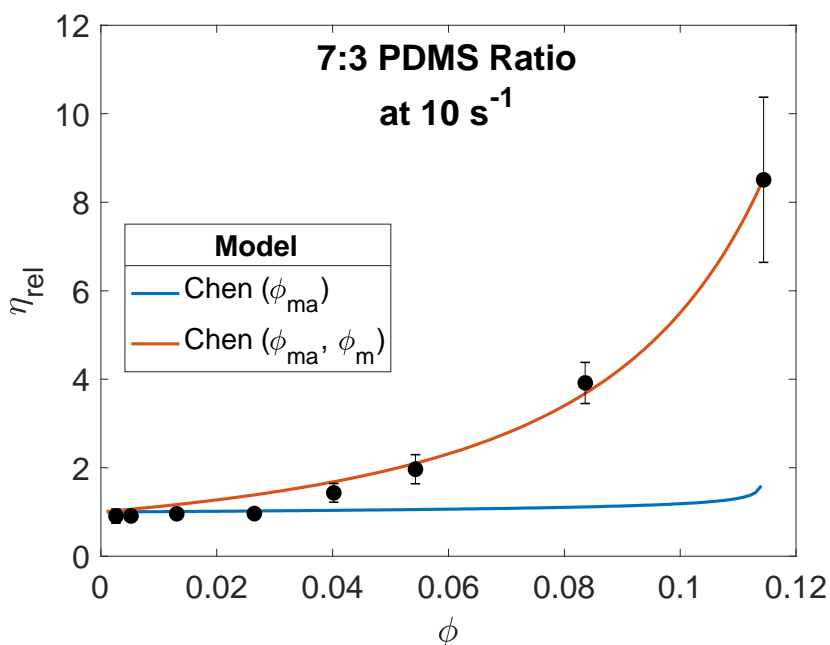


Figure 28: Discrepancy between the fitting of only  $\phi_{ma}$  with both  $\phi_{ma}$  and  $\phi_m$  for the Chen model to experimental data.

## 2.7 Printability of Samples

The 3D printability of the TIMs by DIW is established by the successfully printable range from literature of 7:3 ratio PDMS to 9:1 ratio PDMS [45]. Figure 29 outlines this viscosity range as well as all combinations of PDMS ratios with filler that fall within the range at a constant shear rate of 10 s<sup>-1</sup>. The 8:2 ratio PDMS with 10 wt. % GNP filler is the absolute maximum viscosity that could be printed with similar settings to 9:1 pure PDMS. The range itself is generated using the fitting of Chen's model with two-parameters as it most closely matches the experimental data especially at high particle loadings. Several of the lower concentration GNP loadings that appear within the range are not printable due to Chen's model not accurately describing their lubricating effect that lowers the viscosity below that of the pure PDMS sample.

Therefore, this range is most accurate at higher GNP loadings. Clearly, adding more Sylgard 184 and lowering the viscosity of the base fluid allows for higher concentrations of GNP to be added that will give better thermal conductivity with the same DIW processing parameters. The data does appear to plateau at PDMS ratios of 6:4 and 5:5 which can be attributed to the exceedingly large enhancement that occurs at particle loadings above 0.08-0.1 vol. concentrations. The nanocomposites show a consistent enhancement in viscosity at the highest shear rates tested, but these values would only affect processing at extremely fast throughput rates that is not expected for the prototyping ability of 3D printing.

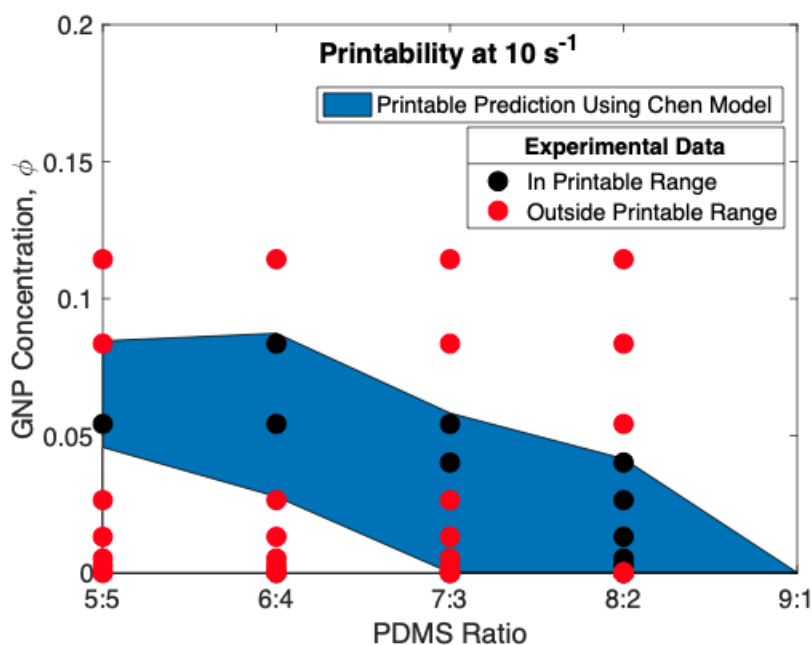


Figure 29: Samples with GNP filler that fall within the printable viscosity range using Chen's model with two fit parameters as well as all experimental data points measured in this work.

## 2.8 Thermal Conductivity Measurement Technique

The thermal conductivity is measured using an IR camera. The sample is suspended between two reference samples of known thermal conductivity. The measurement begins by pouring liquid nitrogen into the top of the device to cool the lens below 78 K. The technique calculates the thermal conductivity of the sample based on the slope of the temperature gradient through the sample, similarly to Fourier's law in Equation (2), so a steady state temperature profile is required. This temperature gradient is created with an electronic heater giving a

constant heat flux on one side of the sample and a water-cooling setup on the other side. The IR camera measures the emissivity for a constant temperature profile followed by three measurements of increasing temperature gradients by raising the power of the electronic heater. The IR camera image is post-processed in a MATLAB program which gives both thermal conductivity and contact resistance between the sample and reference layers.

## **2.9 Modeling of Thermal Conductivity**

Thermal conductivity modeling requires obtaining complete experimental data throughout the loading of GNP. The extensive research done on graphene thermal conductivity has proven its superior thermal properties as well as its benefits for implementation into thermal interface materials [61]–[63]. Nan’s model should be able to fit the experimental data due to previous success in modeling thermal conductivity of graphene [64]–[66]. Nan’s model is particularly beneficial as it can account for anisotropy due to filler alignment that has been shown to occur in the 3D printing of similarly shaped fillers [15], [67]. However, if a single model is not a good fit, then multiple-level EMAs, with Li et al. as a basis, can be used to obtain a more accurate model of the data by further accounting for the effect of aggregation in the samples [18]. Thermal conductivity data will give an accurate assessment of the increased performance for the PDMS-GNP nanocomposite with filler addition as a TIM.

### 3. PRINTING OF RADIATIVE COOLING INK

The second polymer-nanocomposite system whose processing capability is examined is radiative cooling paint. The paint medium consists of Elvacite 2028 acrylic resin from Lucite International. This acrylic was chosen due to its low molecular weight corresponding to a low viscosity as well as its compatibility with a large array of solvents. Common uses for this material include flexographic inks, lacquers, and metal coatings. The filler dispersed throughout the matrix is BaSO<sub>4</sub> particles at ~60 vol. %. The pigments were pre-dispersed in a three-pin mixer that was used to break apart any large clusters. The particles scatter away light that falls in the solar spectrum while the acrylic matrix emits heavily through the transparent window in the atmosphere. Together, these optical properties allow the white paint to cool below ambient temperatures even under direct sunlight [2]. Automating application of the paint could reduce costs, eliminate human labor, and allow creation of more intricate and detailed patterns that could be useful in future applications that require thermal gradients at a small scale. However, since the optical properties of this system are imperative for its function, the formulation cannot be significantly altered to aid in processing. In fact, the only adjustable parameters are modification of the type of solvent or increase in the solvent concentration to lower the viscosity of the mixture. The solvent dissolves the acrylic particles and evaporates away after deposition leaving the solid paint coating; therefore, the solvent does not affect optical properties. The objective of this chapter is to select an automated process that can demonstrate the thermal cooling performance of the paint under direct sunlight for the smallest possible length scale.

#### 3.1 Techniques for Printing Ink versus Paint

Identification of a processing technique that could successfully coat patterns or lettering for the radiative cooling paint must begin with a distinction between paint and ink-based systems. Paints consist of a pigment particle inside of an acrylic or oil medium. On the other hand, ink only contains the pigment as well as possible additives depending on the printing method. Inks are often several orders of magnitude lower viscosity compared to paints. Paints are typically processed using spray coating, spin coating, or simple brush-painting while popular ink-based techniques include inkjet or laser printing.

### 3.1.1 Brush Coating

The simplest paint application method is brush coating. This involves directly applying the radiative cooling paint to a surface with a paint brush by-hand in the same way someone would paint the walls in their home. The technique does not require long-term stability of the paint as application can be done immediately after thoroughly mixing the sample. The primary benefit of this method is the extremely low cost, quick setup time, and little expertise needed for its use. This procedure has been previously used for nanocomposite systems including those of optical relevance for organic solar cells [68]. In fact, the particle alignment caused from shear stress during brushing has shown a higher power conversion efficiency when compared with spray-coated samples [69]. However, brush coating is not automated and requires increased human labor compared to automated methods. The lack of automation also limits the scale of coatings to large enough patterns that can be taped off by-hand.

### 3.1.2 Inkjet

The most common commercial processing technique for ink-based system is an inkjet printer. Unlike laser printers which have higher resolutions, inkjet printers do not require additional electrostatic additives to the ink. Instead, the only requirements for the solution are a relatively low viscosity and fast solvent evaporation after deposition. The main characteristic of inkjet printing is that the ink is deposited onto the substrate in single droplets that are created from thermal, mechanical, or electrostatic deformation [70]. Mechanical deformation is chosen for this paint application due to the greater degree of freedom in designing ink composition since high temperature stability or electrical conduction are not required. The resolution can extend into the micrometer range which is a significantly greater resolution than can be achieved with brush coating by-hand [71]. The process is proven for use in nanofluid systems [72], [73] with similar particle dimensions to BaSO<sub>4</sub> as well as nanocomposite systems with an acrylic matrix [74].

### 3.1.3 Screen Printing

Screen printing involves pressing paint through a fine mesh material. A pattern is generated by creating a computer stencil and filling all open mesh outside of the desired printing area with photopolymer that is cured with UV light. The resolution of the technique varies based

on the mesh spacing which can easily be altered by implementing a different screen. Common applications of screen printing include the lettering or logos on clothing as well as lettering on printed circuit boards. The benefit to screen printing is that there is no viscosity requirement if the paint can be forced through the mesh. The method is easier to employ than inkjet printing while providing much higher resolutions than any other type of human-based applications.

### 3.2 Nanocomposite Printing of Radiative Cooling Paint

Inkjet printing is the first method tested for automated processing of radiative cooling paint due to the ease of transition from a laboratory to commercial setting. The drop-on-demand inkjet printing setup used in this work can be seen below in Fig. 30. The sample is contained in a 3 mL syringe with a 500  $\mu\text{m}$  diameter nozzle. The syringe is fixed in position while a computer-controlled build stage moves the substrate to create the desired pattern. The droplets are formed by a reciprocating piston that deforms the tip of the syringe nozzle to draw ink out of the syringe. The printing parameters are controlled by the speed and force provided by the piston.

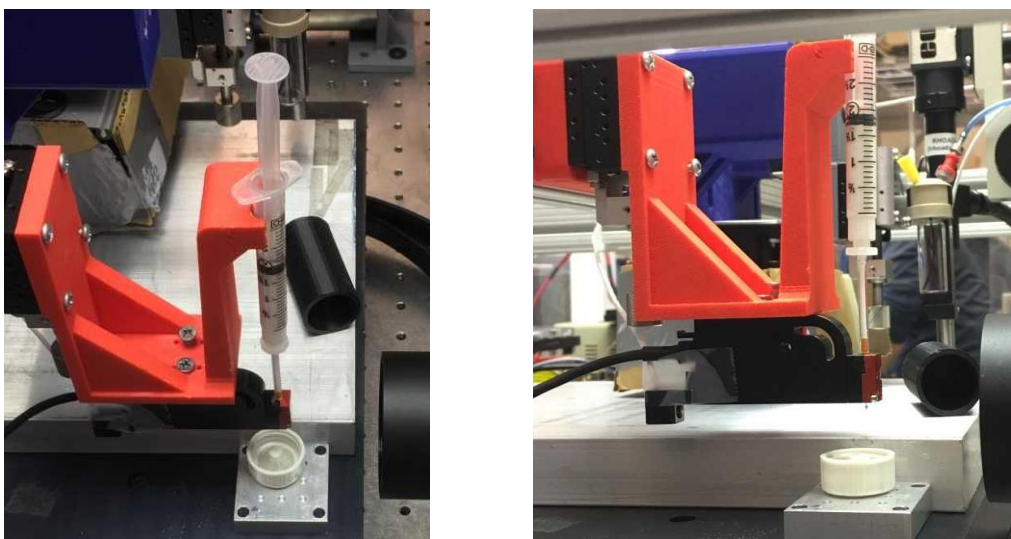


Figure 30: Drop-on-demand inkjet printing setup for radiative cooling paint processing.

Initially, the paint composition is the exact formulation used in previous brush-painting. The paint consists of acrylic,  $\text{BaSO}_4$  particles, and methyl ethyl ketone (MEK) as the solvent. MEK was initially chosen as it has the lowest viscosity for any solvent compatible with the Elvacite 2028 acrylic resin. However, MEK was unable to print any material as the tip of the

syringe dried out before dispensing could begin. Two additional solvents, toluene and dimethylformamide (DMF), were selected with lower evaporation rates as seen in Table 2.

Table 1: Solvent selection parameters.

Solvent	Evaporation Rate	Vapor Pressure (torr) @ 20°C	Viscosity (cP) @ 25°C	Solubility in water @ 20°C
MEK	3.8	70.2	0.40	290 g/L
Toluene	1.9	21.9	0.62	0.526 g/L
DMF	0.2	3.7	0.802	Complete

The solvents in Table 2 have an indirect relationship between evaporation time and viscosity. The evaporation rate is standardized with butyl acetate that is given a rate of one and is directly related to the vapor pressure of the fluid. Toluene is somewhat successfully printed as a continuous stream allows deposition of single droplets, but any break in printing also causes clogging due to the solvent drying out at the tip of the nozzle. DMF resolves the issue of solvent evaporation at the nozzle due to the much slower evaporation rate, but there remained issues with clogging because ~60 vol. % BaSO<sub>4</sub> particles could restrict flow through the nozzle control volume as large aggregates accumulated. Another difficulty with the paint is a very limited stability time due to the large density and concentration of filler particles. This meant that the paint separates in less than an hour after mixing ceases. This stability does not bode well for the inkjet method as commercial inks remain stable for years and particle settling further restricts flow through the nozzle. Dispersive additives including Disperbyk 111 were included in the paint to extend settling times, but the dispersant only extended times by several minutes and affected optical properties meaning that they could not be included at any concentration in the solution.

Screen printing is next implemented to circumvent the problem of clogged nozzles during inkjet testing. The setup to print a Purdue “P” is shown in Fig. 31. The red coating is the photopolymer that blocks paint flow outside of the desired stencil pattern. Several different mesh sizes are tested ranging from 105-310 number or 0.0059-0.0017-inch mesh, which corresponds to a resolution of around 150-50 μm. The tests all included BaSO<sub>4</sub> particles at ~60 vol. % with DMF solvent. The finer meshes blocked much of the paint from passing through the screen, but the larger meshes produced very clean and distinct lettering. The only issue that arose during printing was that the red photopolymer would slowly be dissolved by the DMF and leak into the white paint which caused a red hue to develop after several prints. Thus, the photopolymer was

replaced by a new UV curable polymer that was less susceptible to the DMF solvent in the radiative cooling paint.



Figure 31: Screen printing setup for processing of radiative cooling paint samples.

### 3.3 Radiative Cooling Viscosity

The viscosity of the radiative cooling paint mixture displays much of the expected shear-thinning properties of polymers with nanoscale filler. The viscosity in Pa\*s from  $10^{-2}$  to  $10^3$   $s^{-1}$  shear rates is seen in Fig. 26. The viscosity levels out after a shear rate of  $1$   $s^{-1}$  and remains at a relatively constant value of  $0.0153$  Pa\*s. This value corresponds to the range for ink viscosity used in inkjet printing. However, compared to values of commercial paint in Fig. 27, the radiative cooling paint formulation is a much lower viscosity for all shear rates. Commercial paints have an acrylic matrix, but likely the additional stabilizers and proprietary compounds that allow for years of stability in commercial paints increase the viscosity. Without these compounds, the solvent, which is the primary factor for dilution and the lowering of viscosity, becomes a much higher percentage of the overall composition. The US water-based paint is the only sample that has a viscosity below  $1$  Pa\*s after a shear rate of  $10^2$   $s^{-1}$  and corresponds to the maximum value at very low shear rates measured for the radiative cooling paint.

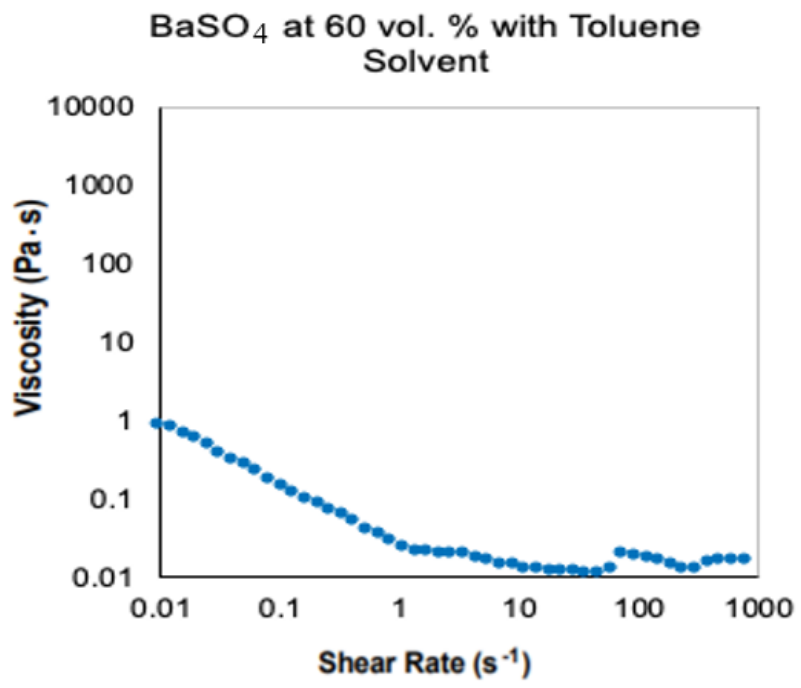


Figure 32: Viscosity as a function of shear rate for the radiative cooling paint sample with 60 vol. % BaSO<sub>4</sub> and toluene solvent.

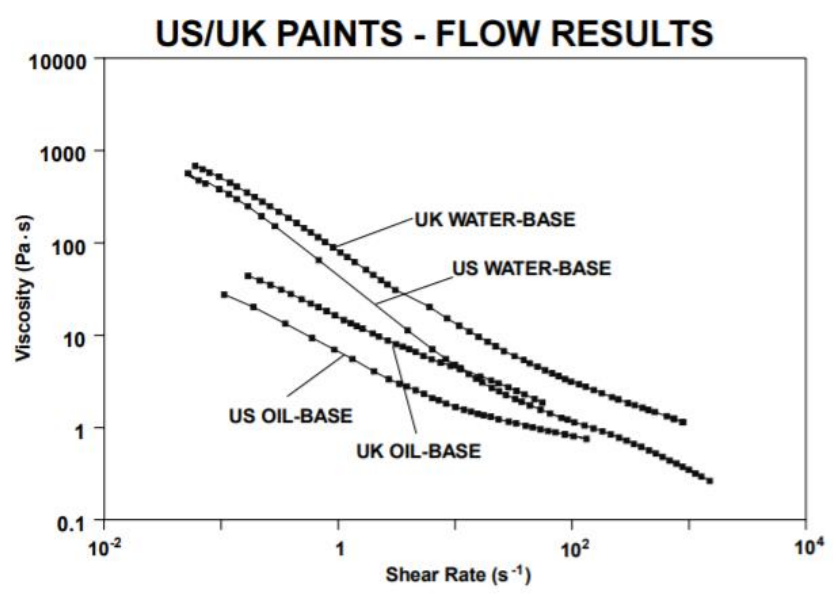


Figure 33: Viscosity as a function of shear rate for commercial paints with different matrix materials [75].

### 3.4 Printed Performance of Radiative Cooling Paint

The radiative cooling paint samples were successfully printed using both inkjet and screen printing. The printed pattern is similar to a Snellen eye chart that transitioned from size 10 to 26 font in increments of 2 in the shape of a “P”. The goal of this pattern was to obtain the lowest font size that could be both invisible to the naked eye, while still being visible and readable by an IR camera image. The screen printing technique is particularly successful at providing a solid and thick coating of paint that would have required several passes from the inkjet nozzle to replicate. The pattern of P’s is applied to two different paper substrates. The first is commercial printer paper and the second is an ultra-white art paper that is coated with a barium sulfate emulsion. The pattern applied by screen printing on the two substrates is shown in Fig. 34. The baryte paper is nearly invisible to the naked eye as seen in Fig. 34a., while the shadow created by the raised edges of the paint on the commercial paper make it clearer as seen in Fig. 34b.

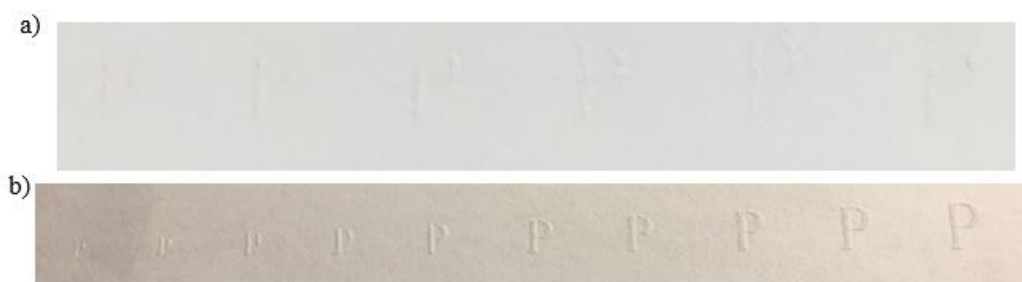


Figure 34: Screen printing of radiative cooling paint pattern onto a) barium sulfate coated art paper and b) commercial printer paper.

A temperature difference between the paper substrate and the radiative cooling paint is very difficult to resolve. A Fluke TiS thermal camera is used to both measure the temperature gradient and obtain an image of the optically invisible ink that should provide a temperature difference visible in the IR spectrum. This demonstration of invisible ink has already been demonstrated in our group with the radiative cooling paint surrounded by commercial white paint [2]. However, as is seen in Fig. 35 for screen printing on commercial printer paper, there is no measurable temperature difference between the radiative cooling paint and either paper substrate with inkjet or screen printing. There is a qualitative difference that gives a slight color

variation under the most optimal conditions, but the temperature gradients remain within the  $\pm 2$  °C uncertainty of the IR camera.



Figure 35: IR camera image of the screen-printed radiative cooling paint with very little temperature difference compared to the commercial printing paper substrate.

The lack of a quantitative temperature difference between the radiative cooling paint and paper substrate can be explained by the radiative properties of the substrates themselves. The baryte paper shows over 0.93 reflectance over a large portion of the solar spectrum with significant absorption after wavelengths of 1500 nm as is shown in Fig. 36. The commercial printer paper has a lower reflectance of about 0.80 in the solar spectrum and a similar trend in absorption that becomes significant after wavelengths of 1500 nm as is seen in Fig. 37. However, the lower reflectance is due to the commercial printing paper having higher transmission of around 0.20 throughout the solar spectrum. Since neither substrate has significant absorption in the largest part of the solar spectrum, little to no temperature difference should be expected between the radiative cooling paint and the papers. The temperature gradient compared with a commercial paint substrate is largely due to the ~15% absorption of the commercial white paint in these same wavelengths. Therefore, a substrate with higher absorption in the solar spectrum is required to obtain a visible temperature difference in the IR. Then, the paint will be able to demonstrate the de-coupling of thermal and visual or color effects as an optically invisible white ink that is cooler under direct sunlight. This work is the first to demonstrate successful printing of radiative cooling paint with both inkjet and screen printing procedures.

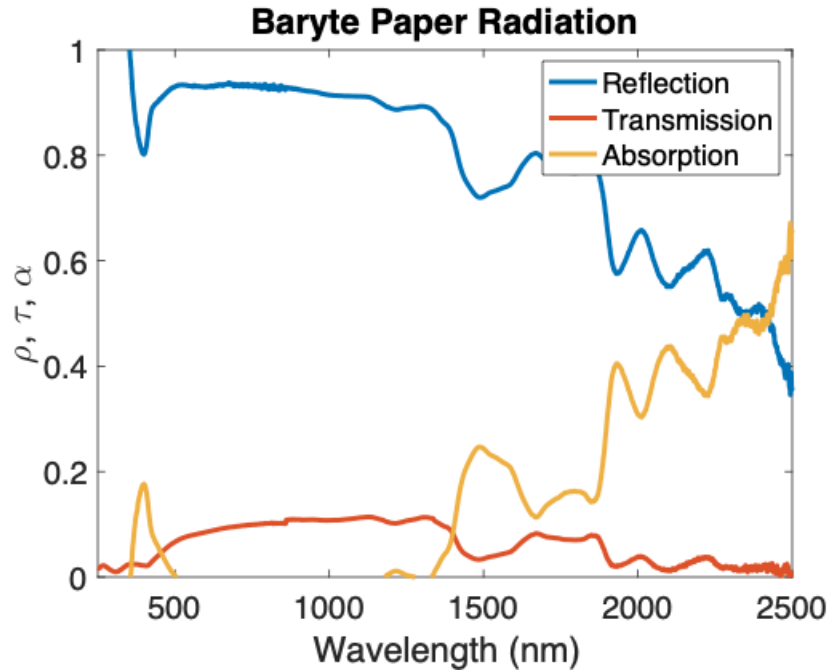


Figure 36: Radiative properties of the baryte paper substrate.

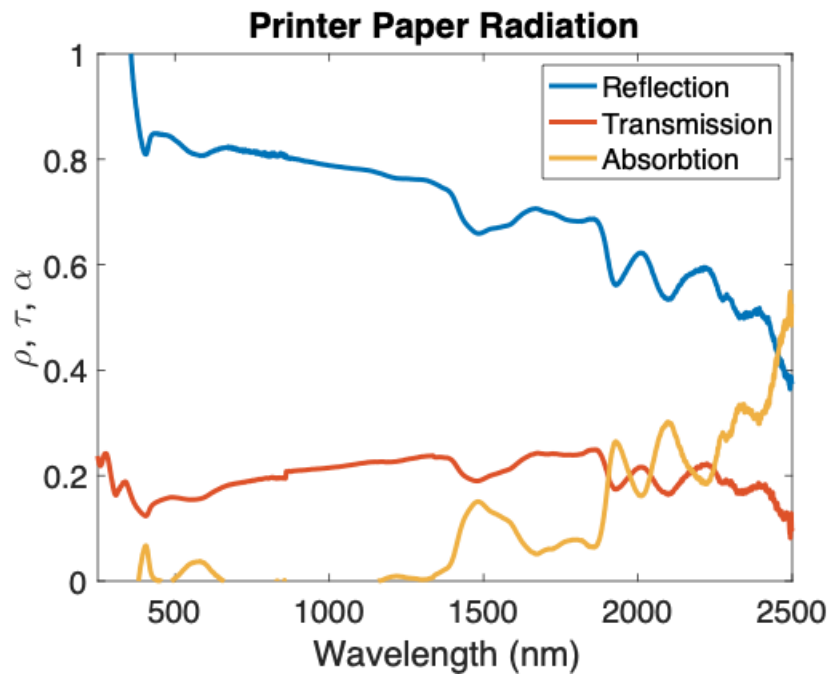


Figure 37: Radiative properties of the commercial printer paper substrate.

## REFERENCES

- [1] V. Prakash Sharma, U. Sharma, M. Chattopadhyay, and V. N. Shukla, “Advance Applications of Nanomaterials: A Review,” *Mater. Today Proc.*, vol. 5, pp. 6376–6380, 2018.
- [2] X. Li, “Engineering Nanocomposites and Interfaces for Conduction and Radiation Thermal Management,” 2019.
- [3] T. S. Fisher, “Lattice Structure, Phonons, and Electrons,” in *Thermal Energy at the Nanoscale*, Danvers, Massachusetts: World Scientific Publishing Co., 2014.
- [4] T. Feng and X. Ruan, “Prediction of Spectral Phonon Mean Free Path and Thermal Conductivity with Applications to Thermoelectrics and Thermal Management: A Review,” *J. Nanomater.*, vol. 2014, pp. 1–25, 2014.
- [5] Z. M. Zhang, *Nano/Microscale Heat Transfer*. New York: McGraw-Hill, 2007.
- [6] D. G. Cahill *et al.*, “Nanoscale thermal transport,” *J. Appl. Phys.*, vol. 93, no. 2, pp. 793–818, 2003.
- [7] P. L. Kapitza, “Heat Transfer and Superfluidity of Helium II,” *Phys. Rev.*, vol. 60, no. 4, pp. 354–355, 1941.
- [8] J. C. Maxwell, “A Treatise on Electricity and Magnetism,” *Oxford: Clarendon Press*. 1873.
- [9] J. C. M. Garnett, “Colours in Metal Glasses and in Metallic Films,” *Phil. Trans., A*, vol. 203, pp. 385–420, 1904.
- [10] R. L. Hamilton and O. K. Crosser, “Thermal Conductivity of Heterogeneous Two-Component Systems,” *Ind. Eng. Chem. Fundam.*, vol. 1, no. 3, pp. 187–191, 1962.
- [11] D. P. H. Hasselman and L. F. Johnson, “Effective Thermal Conductivity of Composites with Interfacial Thermal Barrier Resistance,” *J. Compos. Mater.*, vol. 21, pp. 508–515, 1987.
- [12] R. Prasher, “Thermal Interface Materials: Historical Perspective, Status, and Future Directions,” *Proc. IEEE*, vol. 94, no. 8, pp. 1571–1586, 2006.
- [13] Z. Hashin and S. Shtrikman, “A Variational Approach to the Theory of the Effective Magnetic Permeability of Multiphase Materials,” *J. Appl. Phys.*, vol. 33, no. 10, pp. 3125–3131, 1962.

- [14] C. Pan, K. Kou, Y. Zhang, Z. Li, and G. Wu, "Enhanced through-plane thermal conductivity of PTFE composites with hybrid fillers of hexagonal boron nitride platelets and aluminum nitride particles," *Compos. Part B Eng.*, vol. 153, no. July, pp. 1–8, 2018.
- [15] C. W. Nan, R. Birringer, D. R. Clarke, and H. Gleiter, "Effective Thermal Conductivity of Particulate Composites with Interfacial Thermal Resistance," *J. Appl. Phys.*, vol. 81, no. 10, pp. 6692–6699, 1997.
- [16] W. Evans, R. Prasher, J. Fish, P. Meakin, P. Phelan, and P. Keblinski, "Effect of Aggregation and Interfacial Thermal Resistance on Thermal Conductivity of Nanocomposites and Colloidal Nanofluids," *Int. J. Heat Mass Transf.*, vol. 51, pp. 1431–1438, 2008.
- [17] D. A. G. Bruggeman, "Berechnung verschiedener physikalischer Konstanten von heterogenen Substanzen," vol. 24, no. 5, pp. 636–664, 1935.
- [18] X. Li, W. Park, and Y. P. Chen, "Effect of Particle Size and Aggregation on Thermal Conductivity of Metal-Polymer Nanocomposite," *J. Heat Transfer*, vol. 139, no. 2, 2016.
- [19] R. Pamies, J. G. Hernández Cifre, M. del Carmen López Martínez, and J. García de la Torre, "Determination of Intrinsic Viscosities of Macromolecules and Nanoparticles. Comparison of Single-Point and Dilution Procedures," *Colloid Polym. Sci.*, vol. 286, pp. 1223–1231, 2008.
- [20] M. L. Huggins and V. 64, "The Viscosity of Dilute Solutions of Long-Chain Molecules. IV. Dependence on Concentration," *J. Am. Chem. Soc.*, vol. 64, pp. 2716–2718, 1942.
- [21] E. O. Kraemer, "Molecular Weights of Celluloses," *Ind. Eng. Chem.*, vol. 30, no. 10, pp. 1200–1203, 1938.
- [22] O. F. Solomon and I. Z. Ciuta, "Détermination De La Viscosité Intrinsèque De Solutions De Polymères Par Une Simple Détermination De La Viscosité.," *Appl. Polym. Sci.*, vol. 6, no. 24, pp. 683–686, 1962.
- [23] A. Einstein, "A Determination of Molecular Dimensions," *Ann. Phys.*, vol. 4, no. 19, pp. 37–62, 1906.
- [24] G. K. Batchelor, "Effect of Brownian-motion on Bulk Stress in a Suspension of Spherical-particles," *J. Fluid Mech.*, vol. 83, pp. 97–117, 1977.
- [25] B. M. Haines and A. L. Mazzucato, "A Proof of Einstein's Effective Viscosity for a Dilute Suspension of Spheres," *SIAM J. Math. Anal.*, vol. 44, no. 3, pp. 2120–2145, 2012.

- [26] I. M. Krieger and T. J. Dougherty, "A Mechanism for Non-Newtonian Flow in Suspensions of Rigid Spheres," *J. Rheol. (N. Y. N. Y.)*, vol. 3, no. 1, pp. 137–152, 1959.
- [27] J. P. Meyer, S. a. Adio, M. Sharifpur, and P. N. Nwosu, "The viscosity of nanofluids: a review of the theoretical, empirical and numerical models," *Heat Transf. Eng.*, vol. 7632, no. JUNE, pp. 00–00, 2015.
- [28] H. Chen, Y. Ding, and C. Tan, "Rheological behaviour of nanofluids," *New J. Phys.*, vol. 9, 2007.
- [29] H. Chen, Y. Ding, and A. Lapkin, "Rheological behaviour of nanofluids containing tube / rod-like nanoparticles," *Powder Technol.*, vol. 194, pp. 132–141, 2009.
- [30] A. L. Moore and L. Shi, "Emerging Challenges and Materials for Thermal Management of Electronics," *Mater. Today*, vol. 17, no. 4, 2014.
- [31] N. Bhattacharjee, A. Urrios, S. Kang, and A. Folch, "The upcoming 3D-printing revolution in microfluidics," *Lab Chip*, vol. 16, no. 10, pp. 1711–1742, 2016.
- [32] A. C. M. Kuo, *Polymer Data Handbook*. 1999.
- [33] S. Hwang, E. I. Reyes, K. Moon, R. C. Rumpf, and N. S. Kim, "Thermo-mechanical Characterization of Metal/Polymer Composite Filaments and Printing Parameter Study for Fused Deposition Modeling in the 3D Printing Process," *J. Electron. Mater.*, vol. 44, no. 3, pp. 771–777, 2015.
- [34] V. Saggiomo and A. H. Velders, "Simple 3D Printed Scaffold-Removal Method for the Fabrication of Intricate Microfluidic Devices," *Adv. Sci.*, vol. 2, 2015.
- [35] R. D. Farahani, M. Dubé, and D. Therriault, "Three-Dimensional Printing of Multifunctional Nanocomposites: Manufacturing Techniques and Applications," *Adv. Mater.*, vol. 28, pp. 5794–5821, 2016.
- [36] T. J. Hinton, A. Hudson, K. Pusch, A. Lee, and A. W. Feinberg, "3D Printing PDMS Elastomer in a Hydrophilic Support Bath via Freeform Reversible Embedding," *ACS Biomater. Sci. Eng.*, vol. 2, pp. 1781–1786, 2016.
- [37] J. Z. Manapat, Q. Chen, P. Ye, and R. C. Advincula, "3D Printing of Polymer Nanocomposites via Stereolithography," *Macromol. Mater. Eng.*, vol. 302, 2017.
- [38] G. Comina, A. Suska, and D. Filippini, "PDMS lab-on-a-chip fabrication using 3D printed templates," *R. Soc. Chem.*, vol. 14, pp. 424–430, 2014.
- [39] T. Femmer, A. J. C. Kuehne, J. Torres-Rendon, A. Walther, and M. Wessling, "Print your

- membrane: Rapid prototyping of complex 3D-PDMS membranes via a sacrificial resist,” *J. Memb. Sci.*, vol. 478, pp. 12–18, 2015.
- [40] R. L. Truby and J. A. Lewis, “Printing soft matter in three dimensions,” *Nature*, vol. 540, pp. 371–378, 2016.
- [41] J. A. Lewis, “Direct Ink Writing of 3D Functional Materials,” *Adv. Funct. Mater.*, vol. 16, pp. 2193–2204, 2006.
- [42] N. Nguyen, E. Melamed, J. G. Park, S. Zhang, A. Hao, and R. Liang, “Direct Printing of Thermal Management Device Using Low-Cost Composite Ink,” *Macromol. Mater. Eng.*, 2017.
- [43] S. Roh, D. P. Parekh, B. Bharti, S. D. Stoyanov, and O. D. Velev, “3D Printing by Multiphase Silicone/Water Capillary Inks,” *Adv. Mater.*, 2017.
- [44] S. Shan *et al.*, “Multistable Architected Materials for Trapping Elastic Strain Energy,” *Adv. Mater.*, vol. 27, no. 29, pp. 4296–4301, 2015.
- [45] V. Ozbolat, M. Dey, B. Ayan, A. Povilianskas, M. C. Demirel, and I. T. Ozbolat, “3D Printing of PDMS Improves Its Mechanical and Cell Adhesion Properties,” *ACS Biomater. Sci. Eng.*, vol. 4, pp. 682–693, 2018.
- [46] J. Jeong, C. Li, Y. Kwon, J. Lee, S. H. Kim, and R. Yun, “Particle shape effect on the viscosity and thermal conductivity of ZnO nanofluids,” *Int. J. Refrig.*, vol. 36, pp. 2233–2241, 2013.
- [47] Gaganpreet and S. Srivastava, “Viscosity of nanofluids: particle shape and fractal aggregates,” *Phys. Chem. Liq.*, vol. 53, no. 2, pp. 174–186, 2015.
- [48] S. Mueller, E. Llewellyn, H. M. Mader, S. Mueller, and E. W. Llewellyn, “The effect of particle shape on suspension viscosity and implications for magmatic flows,” *Artic. Geophys. Res. Lett.*, vol. 38, 2011.
- [49] Y. Li, M. Krö, and W. K. Liu, “Nanoparticle Geometrical Effect on Structure, Dynamics and Anisotropic Viscosity of Polyethylene Nanocomposites,” *Macromolecules*, vol. 45, pp. 2099–2112, 2012.
- [50] Z. He *et al.*, “Effect of the Filler Structure of Carbon Nanomaterials on the Electrical, Thermal, and Rheological Properties of Epoxy Composites,” *J. Appl. Polym. Sci.*, pp. 3366–3372, 2013.
- [51] S. T. Knauert, J. F. Douglas, and F. W. Starr, “The Effect of Nanoparticle Shape on

- Polymer-Nanocomposite Rheology and Tensile Strength,” *J. Polym. Sci. Part B Polym. Phys.*, vol. 45, pp. 1882–1897, 2007.
- [52] E. V. Timofeeva, J. L. Routbort, and D. Singh, “Particle shape effects on thermophysical properties of alumina nanofluids,” *J. Appl. Phys.*, vol. 106, 2009.
- [53] E. Sadeghinezhad *et al.*, “A comprehensive review on graphene nanofluids: Recent research, development and applications,” *Energy Convers. Manag.*, vol. 111, pp. 466–487, 2016.
- [54] M. B. Moghaddam, E. K. Goharshadi, M. H. Entezari, and P. Nancarrow, “Preparation, characterization, and rheological properties of graphene-glycerol nanofluids,” *Chem. Eng. J.*, vol. 231, pp. 365–372, 2013.
- [55] M. Mehrali *et al.*, “Effect of specific surface area on convective heat transfer of graphene nanoplatelet aqueous nanofluids,” *Exp. Therm. Fluid Sci.*, vol. 68, pp. 100–108, 2015.
- [56] C. E. Wagner, A. C. Barbati, J. Engmann, A. S. Burbidge, and G. H. McKinley, “Apparent Shear Thickening at Low Shear Rates in Polymer Solutions Can Be an Artifact of Non-equilibration,” *Appl. Rheol.*, vol. 26, pp. 1–5, 2016.
- [57] A. V. Shenoy, *Rheology of Filled Polymer Systems*. 1999.
- [58] B. Lai and X. Ni, “Rheological Behavior and Interaction of Polycarbonate/Barium Sulfate Composites,” *J. Macromol. Sci. Part B Phys.*, vol. 47, pp. 1028–1038, 2008.
- [59] L. Raeisian, J. R. Eggers, E. M. Lange, T. Mattke, A. Bode, and S. Kabelac, “On the Controversy of Nanofluid Rheological Behavior,” *Int. J. Thermophys.*, vol. 40, no. 5, p. 48, 2019.
- [60] P. Chen, J. Zhang, and J. He, “Increased Flow Property of Polycarbonate by Adding Hollow Glass Beads,” *Polym. Eng. Sci.*, vol. 45, no. 8, pp. 1119–1131, 2005.
- [61] B. Li and W.-H. Zhong, “Review on polymer/graphite nanoplatelet nanocomposites,” *J. Mater. Sci.*, vol. 46, pp. 5595–5614, 2011.
- [62] A. A. Balandin *et al.*, “Superior Thermal Conductivity of Single-Layer Graphene,” *Nano Lett.*, vol. 8, no. 3, pp. 902–907, 2008.
- [63] S. Ghosh *et al.*, “Extremely High Thermal Conductivity of Graphene: Prospects for Thermal Management Applications in Nanoelectronic Circuits,” *Appl. Phys. Lett.*, vol. 92, pp. 1–3, 2008.
- [64] W. Park *et al.*, “High-Performance Thermal Interface Material Based on Few-Layer

- Graphene Composite,” 2015.
- [65] X. Shen, Z. Wang, Y. Wu, X. Liu, Y. B. He, and J. K. Kim, “Multilayer Graphene Enables Higher Efficiency in Improving Thermal Conductivities of Graphene/Epoxy Composites,” *Nano Lett.*, vol. 16, no. 6, pp. 3585–3593, 2016.
- [66] K. M. F. Shahil and A. A. Balandin, “Graphene–Multilayer Graphene Nanocomposites as Highly Efficient Thermal Interface Materials,” *Nano Lett.*, vol. 12, p. 57, 2012.
- [67] J. Liu, W. Li, Y. Guo, H. Zhang, and Z. Zhang, “Improved thermal conductivity of thermoplastic polyurethane via aligned boron nitride platelets assisted by 3D printing,” *Compos. Part A Appl. Sci. Manuf.*, vol. 120, no. February, pp. 140–146, 2019.
- [68] J. A. Jeong, Y. J. Jeon, S. S. Kim, B. Kyoung Kim, K. B. Chung, and H. K. Kim, “Simple brush-painting of Ti-doped In<sub>2</sub>O<sub>3</sub> transparent conducting electrodes from nano-particle solution for organic solar cells,” *Sol. Energy Mater. Sol. Cells*, 2014.
- [69] S. S. Kim, S. I. Na, J. Jo, G. Tae, and D. Y. Kim, “Efficient polymer solar cells fabricated by simple brush painting,” *Adv. Mater.*, vol. 19, pp. 4410–4415, 2007.
- [70] S. Magdassi, “Ink Requirements and Formulations Guidelines,” in *Chemistry of Inkjet Inks*, 2010, pp. 19–41.
- [71] M. Singh, H. M. Haverinen, P. Dhagat, and G. E. Jabbour, “Inkjet printing-process and its applications,” *Adv. Mater.*, vol. 22, pp. 673–685, 2010.
- [72] H. H. Lee, K. Sen Chou, and K. C. Huang, “Inkjet printing of nanosized silver colloids,” *Nanotechnology*, 2005.
- [73] D. J. Finn *et al.*, “Inkjet deposition of liquid-exfoliated graphene and MoS<sub>2</sub> nanosheets for printed device applications,” 2013.
- [74] R. Giardi, S. Porro, A. Chiolerio, E. Celasco, and M. Sangermano, “Inkjet printed acrylic formulations based on UV-reduced graphene oxide nanocomposites,” *J. Mater. Sci.*, vol. 48, pp. 1249–1255, 2013.
- [75] P. Whittingstall, “PAINT EVALUATION USING RHEOLOGY.”